PROCEEDINGS A

royalsocietypublishing.org/journal/rspa

Research

Cite this article: Ball TV, Balmforth NJ. 2021 Viscoplastic plates. *Proc. R. Soc. A* **477**: 20210509.
https://doi.org/10.1098/rspa.2021.0509

Received: 22 June 2021
Accepted: 9 September 2021

Subject Areas:
applied mathematics, mechanics

Keywords:
plates, plasticity, viscoplastic

Author for correspondence:
Thomasina V. Ball
e-mail: Thomasina.Ball@warwick.ac.uk

Electronic supplementary material is available online at https://doi.org/10.6084/m9.figshare.c.5632681.

THE ROYAL SOCIETY PUBLISHING

Viscoplastic plates

Thomasina V. Ball[1] and Neil J. Balmforth[2]

[1]Mathematics Institute, University of Warwick, Coventry, CV4 7AL, UK
[2]Department of Mathematics, University of British Columbia, 1984 Mathematics Road, Vancouver, British Columbia, Canada V6T 1Z2

TVB, 0000-0001-8547-0586; NJB, 0000-0002-1534-9104

An asymptotic model is constructed to describe the bending of thin sheets, or plates, of viscoplastic fluid described by the Herschel–Bulkley constitutive law, which incorporates the von Mises yield condition and a nonlinear viscous stress. The model reduces to a number of previous ones from plasticity theory and viscous fluid mechanics in various limits. It is characterized by a yield criterion proposed by Ilyushin which compactly combines the effect of the bending moment and in-plane stress tensors through three particular invariants. The model is used to explore the bending of loaded flat plates, the deflection of impulsively driven circular plates, and the tension-controlled deflection of loaded beams.

1. Introduction

The theory of plates and shells plays a classical role in solid mechanics, combining the expedient simplifications afforded by a slender geometry with a host of important applications [1]. Mining the same vein in the 1950s and 1960s, significant work was devoted to the exploration of the failure of plastic plates (e.g. [2–7]). The link between Stokes flow and linear elasticity further led to development of theories of viscous plates and shells, together with investigations of the fluid analogues of classical bending problems from solid mechanics [8–16]. More recently, the bending dynamics of two-dimensional sheets of viscoplastic fluid have been considered [17–20], combining aspects of all three of these physical problems.

The goal of the present work is to provide a model for the bending of (three-dimensional) plates of viscoplastic fluid characterized by the Herschel–Bulkley constitutive law, a popular model for viscoplastic fluids [21]. To derive this model, we perform an asymptotic analysis of the full three-dimensional governing equations, including tension and stretching within the plane of the plate. The theory follows on from discussion of the two-dimensional bending of viscoplastic sheets [18].

However, we include only the leading-order effects of in-plane stretching, implying that the plate maintains almost constant thickness, and consider relatively low curvatures (both of which limitations could, in principle, be relaxed).

When the deformation rates become small, our model reduces to that for a perfectly rigid-plastic plate satisfying the von Mises yield criterion. However, our inclusion of in-plane tension and stretching generalizes the classical analyses from the plasticity literature [2–4,7,22], which only included bending. The combination of bending moments with in-plane tensions leads to a significantly richer yielding criterion equivalent to that presented by Ilyushin [23,24]. Moreover, the inclusion of viscous stresses furnishes the state of collapse beyond the plastic limit (i.e. the form of motion once one exceeds the critical load for failure). Our theory bears some similarities with earlier work in the plasticity literature incorporating rate-dependent stresses [25–29]. However, unlike that earlier work, our analysis establishes a consistent asymptotic model that we explore in its full form, rather than working with any linearization of the constitutive law.

Although viscoplastic models have been proposed previously for metal plates (e.g. [25–27,29]), our current motivation stems from some geophysical problems. In particular, a viscoplastic plate model may be relevant for describing the deformation of the stiff crust encasing lava and mud flows (e.g. [30–32]). Similarly, the effective viscoplasticity of sea ice can impact its large-scale deformation and the propagation of ocean waves [33,34]. The damping of wave motion by the bending of a viscoplastic surface layer also features in more commonplace or industrial settings [35].

To illustrate the dynamics captured by the thin-plate model, we consider a number of examples motivated by classical plasticity literature. First, we consider the bending of flat, clamped, rectangular plates without tension, constructing the collapse states beyond the initiation of plastic failure (as determined previously by limit analysis [7,22,36–38]). We then consider clamped circular plates (cf. [3,25–27,39,40]) and include in-plane stretching in the dynamics of a loaded plastic beam [17,18]. For some of these examples, we compute solutions using an augmented Lagrangian scheme developed for viscoplastic fluids [41,42]. This scheme computes stress solutions everywhere, including the plug regions where the stress state is formally indeterminate, with the iterative algorithm converging to an admissible stress state. As the implementation of this algorithm for our plate equations is somewhat novel, we provide details in appendix A.

2. Viscoplastic plate model

(a) Formulation

Consider a thin plate of viscoplastic fluid satisfying the Herschel–Bulkley constitutive law (figure 1). The characteristic thickness $\mathcal{H}$ of the plate is much smaller than a characteristic lengthscale $\mathcal{L}$ for bending; $\epsilon = \mathcal{H}/\mathcal{L} \ll 1$. In the Cartesian coordinates, (x, y, z), in which the plate is aligned primarily with the horizontal x–y plane, the governing equations for an incompressible fluid with velocity field $\boldsymbol{u} = (u, v, w)$ are

$$\nabla \cdot \boldsymbol{u} = 0 \tag{2.1}$$

and

$$\rho\left(\frac{\partial \boldsymbol{u}}{\partial t} + \boldsymbol{u}\cdot\nabla\boldsymbol{u}\right) = -\nabla p + \nabla\cdot\boldsymbol{\tau} + \rho\mathbf{g} = \nabla\cdot\boldsymbol{\sigma} + \rho\mathbf{g}, \tag{2.2}$$

where ρ and $\mathbf{g} = (0, 0, -g)$ are density and gravity, and the total stress tensor $\boldsymbol{\sigma} = \boldsymbol{\tau} - p\boldsymbol{I}$ is broken down into the deviatoric stress tensor $\boldsymbol{\tau}$ and pressure p. The Herschel–Bulkley constitutive law is

and

$$\left.\begin{aligned} \dot{\boldsymbol{\gamma}} &= \mathbf{0}, \quad \tau < \tau_Y \\ \boldsymbol{\tau} &= \left(K\dot{\gamma}^{n-1} + \frac{\tau_Y}{\dot{\gamma}}\right)\dot{\boldsymbol{\gamma}}, \quad \tau \geq \tau_Y, \end{aligned}\right\} \tag{2.3}$$

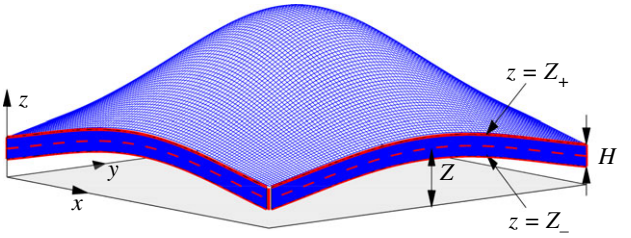

Figure 1. Sketch of the plate geometry. (Online version in colour.)

where τ_Y, K and n represent the yield stress, consistency and power-law index, respectively, and

$$\dot{\gamma}_{jk} = \frac{\partial u_j}{\partial x_k} + \frac{\partial u_k}{\partial x_j}, \quad \dot{\gamma} = \sqrt{\frac{1}{2}\sum_{j,k}\dot{\gamma}_{jk}^2}, \quad \tau = \sqrt{\frac{1}{2}\sum_{j,k}\tau_{jk}^2}. \tag{2.4}$$

At the surfaces of the plate, $z = Z_\pm(x, y, t)$, we have the kinematic and stress conditions,

$$\frac{\partial Z_\pm}{\partial t} + u\frac{\partial Z_\pm}{\partial x} + v\frac{\partial Z_\pm}{\partial y} = w, \quad (\boldsymbol{\tau} - p\boldsymbol{I})\cdot\boldsymbol{n} = N_\pm \boldsymbol{n}, \tag{2.5}$$

where $\boldsymbol{n}$ is the outward normal unit vector, and $N_\pm$ denotes any normal force, including that of surface tension.

(b) Scaling

Following [18], we remove dimensions from the equations by scaling x and y by $\mathcal{L}$, and vertical lengths by $\mathcal{H}$. In the bending-dominated regime, the components of the velocity and stress must be scaled differently. In particular, using the thin sheet approximation and balancing gradients of the stress components in the momentum equation (2.2) [1,12,18], we set

$$(u, v) = \epsilon\mathcal{V}(\hat{u}, \hat{v}), \quad w = \mathcal{V}\hat{w}, \tag{2.6}$$

and

$$(p, \sigma_{xx}, \sigma_{yy}, \sigma_{xy}) = \mathcal{P}(\hat{p}, \hat{\sigma}_{xx}, \hat{\sigma}_{yy}, \hat{\sigma}_{xy}), \quad (\sigma_{xz}, \sigma_{yz}) = \epsilon\mathcal{P}(\hat{\sigma}_{xz}, \hat{\sigma}_{yz}), \quad \sigma_{zz} = \epsilon^2\mathcal{P}\hat{\sigma}_{zz}, \tag{2.7}$$

where $\mathcal{V}$ and $\mathcal{P}$ are characteristic velocity and stress scales. Time is scaled so that $t = (\mathcal{H}/\mathcal{V})\hat{t}$.

In view of these scalings, we may rewrite the continuity and momentum equations in (2.1)–(2.3) as, after dropping the tilde decoration:

$$\frac{\partial u}{\partial x} + \frac{\partial v}{\partial y} + \frac{1}{\epsilon^2}\frac{\partial w}{\partial z} = 0, \tag{2.8}$$

$$O(\epsilon^2) = \frac{\partial \sigma_{xx}}{\partial x} + \frac{\partial \sigma_{xy}}{\partial y} + \frac{\partial \sigma_{xz}}{\partial z}, \quad O(\epsilon^2) = \frac{\partial \sigma_{xy}}{\partial x} + \frac{\partial \sigma_{yy}}{\partial y} + \frac{\partial \sigma_{yz}}{\partial z}, \tag{2.9}$$

$$Re\left(\frac{\partial w}{\partial t} + w\frac{\partial w}{\partial z}\right) = \frac{\partial \sigma_{xz}}{\partial x} + \frac{\partial \sigma_{yz}}{\partial y} + \frac{\partial \sigma_{zz}}{\partial z} - G + O(\epsilon), \tag{2.10}$$

$$\begin{pmatrix} \tau_{xx} & \tau_{xy} & \epsilon\tau_{xz} \\ \tau_{xy} & \tau_{yy} & \epsilon\tau_{yz} \\ \epsilon\tau_{xz} & \epsilon\tau_{yz} & -\tau_{xx} - \tau_{yy} \end{pmatrix} = \left(\dot{\gamma}^{n-1} + \frac{\mathrm{Bi}}{\dot{\gamma}}\right)\dot{\boldsymbol{\gamma}} \tag{2.11}$$

$$\dot{\boldsymbol{\gamma}} = \begin{pmatrix} 2\partial u/\partial x & \partial v/\partial x + \partial u/\partial y & \epsilon^{-1}(\partial u/\partial z + \partial w/\partial x) \\ \partial v/\partial x + \partial u/\partial y & 2\partial v/\partial y & \epsilon^{-1}(\partial v/\partial z + \partial w/\partial y) \\ \epsilon^{-1}(\partial u/\partial z + \partial w/\partial x) & \epsilon^{-1}(\partial v/\partial z + \partial w/\partial y) & 2\epsilon^{-2}\partial w/\partial z \end{pmatrix}, \tag{2.12}$$

royalsocietypublishing.org/journal/rspa Proc. R. Soc. A 477: 20210509

where

$$\mathcal{P}=K\left(\frac{\mathcal{H}\mathcal{V}}{\mathcal{L}^2}\right)^n,\quad Re=\frac{\rho\mathcal{V}^2\mathcal{L}^2}{\mathcal{H}^2\mathcal{P}},\quad G=\frac{\rho g\mathcal{L}^2}{\mathcal{H}\mathcal{P}},\quad \mathrm{Bi}=\frac{\tau_Y}{\mathcal{P}} \tag{2.13}$$

denote the stress scale and three dimensionless groups corresponding to Reynolds, gravity and Bingham numbers. The surface conditions at $z=Z_\pm$ become

$$\frac{\partial Z_\pm}{\partial t}=w+O(\epsilon^2),\quad \sigma_{xz}-\sigma_{xx}\frac{\partial Z_\pm}{\partial x}-\sigma_{xy}\frac{\partial Z_\pm}{\partial y}=0,\quad \sigma_{yz}-\sigma_{xy}\frac{\partial Z_\pm}{\partial x}-\sigma_{yy}\frac{\partial Z_\pm}{\partial y}=0 \tag{2.14}$$

and

$$\sigma_{zz}-\sigma_{xz}\frac{\partial Z_\pm}{\partial x}-\sigma_{yz}\frac{\partial Z_\pm}{\partial y}=\pm N_\pm+O(\epsilon^2), \tag{2.15}$$

where the normal surface forces have been scaled by $\epsilon^2\mathcal{P}$.

(c) Reduction

To reconcile the different scalings in the continuity equation (2.8), the vertical velocity must be independent of z to leading order so we set $w=W(x,y,t)+\epsilon^2 w_2(x,y,z,t)$. In addition, to balance the strain rate components in equation (2.12), after integrating, we find (cf. [1,12,18])

$$u=U(x,y,t)-(z-Z)\frac{\partial W}{\partial x}\quad\text{and}\quad v=V(x,y,t)-(z-Z)\frac{\partial W}{\partial y}, \tag{2.16}$$

where (U,V) denotes the in-plane velocity along the reference surface $z=Z(x,y,t)$. However, in view of the kinematic conditions in equation (2.14), it is also now evident that the plate bends with little change in thickness, and so $Z_\pm=Z\pm\frac{1}{2}$ and the reference surface is just the midplane of the plate and W is its vertical velocity. The continuity equation now reduces to a relation determining w_2 that we do not need.

With the form for the velocity field given by equation (2.16) the primary stress components may now be written as the rank-two tensor:

$$\begin{pmatrix}\sigma_{xx}&\sigma_{xy}\\ \sigma_{xy}&\sigma_{yy}\end{pmatrix}=\begin{pmatrix}\tau_{xx}&\tau_{xy}\\ \tau_{xy}&\tau_{yy}\end{pmatrix}+(\tau_{xx}+\tau_{yy})\mathbf{I}=\left(\dot\gamma^{n-1}+\frac{\mathrm{Bi}}{\dot\gamma}\right)(\boldsymbol{\Delta}-\zeta\boldsymbol{\Gamma}), \tag{2.17}$$

where $\zeta=z-Z$, two key tensors characterizing the degree of stretching and bending are

$$\boldsymbol{\Delta}=2\mathbf{D}+2\mathrm{Tr}(\mathbf{D})\mathbf{I},\quad \boldsymbol{\Gamma}=2\mathbf{K}+2\mathrm{Tr}(\mathbf{K})\mathbf{I}, \tag{2.18}$$

the planar deformation-rate tensor within the midplane has components

$$\begin{aligned}D_{xx}&=\frac{\partial U}{\partial x}+\frac{\partial Z}{\partial x}\frac{\partial W}{\partial x},\quad D_{yy}=\frac{\partial V}{\partial y}+\frac{\partial Z}{\partial y}\frac{\partial W}{\partial y},\\ D_{xy}&=\frac{1}{2}\left(\frac{\partial U}{\partial y}+\frac{\partial Z}{\partial y}\frac{\partial W}{\partial x}+\frac{\partial V}{\partial x}+\frac{\partial Z}{\partial x}\frac{\partial W}{\partial y}\right),\end{aligned} \tag{2.19}$$

the local curvatures are given by the Hessian matrix:

$$\mathbf{K}=\boldsymbol{\nabla}\boldsymbol{\nabla}W\equiv\begin{pmatrix}\partial^2W/\partial x^2&\partial^2W/\partial x\partial y\\ \partial^2W/\partial x\partial y&\partial^2W/\partial y^2\end{pmatrix}, \tag{2.20}$$

and the planar gradient operation is $\boldsymbol{\nabla}\equiv(\partial/\partial x,\partial/\partial y)$.

royalsocietypublishing.org/journal/rspa Proc. R. Soc. A 477: 20210509

After a little algebra, we find that the leading-order strain rate $\dot{\gamma}$ can be written in the form

$$\dot{\gamma} \approx \sqrt{\dot{\gamma}_{xx}^2 + \dot{\gamma}_{yy}^2 + \dot{\gamma}_{xx}\dot{\gamma}_{yy} + \dot{\gamma}_{xy}^2} = \Gamma\sqrt{(\zeta - \Upsilon)^2 + \alpha^2}, \tag{2.21}$$

where key invariants of the bending rate and stretching rate tensors are combined into the three quantities:

$$\Gamma^2 = \frac{1}{2}[\mathrm{Tr}(\boldsymbol{\Gamma}^2) - \frac{1}{3}\mathrm{Tr}(\boldsymbol{\Gamma})^2] = 4\left[\left(\frac{\partial^2 W}{\partial x^2}\right)^2 + \left(\frac{\partial^2 W}{\partial y^2}\right)^2 + \frac{\partial^2 W}{\partial x^2}\frac{\partial^2 W}{\partial y^2} + \left(\frac{\partial^2 W}{\partial x \partial y}\right)^2\right], \tag{2.22}$$

$$\begin{aligned}\Upsilon &= \frac{\mathrm{Tr}(\boldsymbol{\Delta}\boldsymbol{\Gamma}) - (1/3)\mathrm{Tr}(\boldsymbol{\Delta})\mathrm{Tr}(\boldsymbol{\Gamma})}{2\Gamma^2} \\ &= \frac{4}{\Gamma^2}\left(D_{xx}\frac{\partial^2 W}{\partial x^2} + D_{yy}\frac{\partial^2 W}{\partial y^2} + \frac{D_{yy}}{2}\frac{\partial^2 W}{\partial x^2} + \frac{D_{xx}}{2}\frac{\partial^2 W}{\partial y^2} + D_{xy}\frac{\partial^2 W}{\partial x \partial y}\right)\end{aligned} \tag{2.23}$$

and

$$\alpha^2 = \frac{\mathrm{Tr}(\boldsymbol{\Delta}^2) - (1/3)\mathrm{Tr}(\boldsymbol{\Delta})^2}{2\Gamma^2} - \Upsilon^2 = \frac{4}{\Gamma^2}(D_{xx}^2 + D_{yy}^2 + D_{xx}D_{yy} + D_{xy}^2) - \Upsilon^2. \tag{2.24}$$

Note that one can show that $\alpha^2 \geq 0$. Thus, the strain rate invariant cannot vanish within the plate unless $\alpha = 0$ and $\zeta = \Upsilon$ simultaneously, which in general identify degenerate points with no particular significance. One can show that the condition $\alpha = 0$ demands that $\mathbf{D} = \Upsilon\mathbf{K}$; if this tensor alignment occurs over a finite area of the plate, the stage is set for stress jumps across the 'neutral surface' $\zeta = \Upsilon$ as in the two-dimensional problem considered in [18]. Aside from such a special situation, the plate must yield as a whole unless $\Gamma = 0$, in which case it is rigid throughout.

Defining the stress resultants:

$$\boldsymbol{\Sigma} = \begin{pmatrix}\Sigma_{xx} & \Sigma_{xy} \\ \Sigma_{xy} & \Sigma_{yy}\end{pmatrix} = \int_{-(1/2)}^{1/2}\begin{pmatrix}\sigma_{xx} & \sigma_{xy} \\ \sigma_{xy} & \sigma_{yy}\end{pmatrix}\mathrm{d}\zeta, \tag{2.25}$$

we may now construct the equations for integral force balance:

$$0 = \frac{\partial}{\partial x}\Sigma_{xx} + \frac{\partial}{\partial y}\Sigma_{xy}, \quad 0 = \frac{\partial}{\partial x}\Sigma_{xy} + \frac{\partial}{\partial y}\Sigma_{yy} \tag{2.26}$$

and

$$Re\frac{\partial W}{\partial t} = \frac{\partial}{\partial x}\int_{-(1/2)}^{1/2}\sigma_{xz}\,\mathrm{d}\zeta + \frac{\partial}{\partial y}\int_{-(1/2)}^{1/2}\sigma_{yz}\,\mathrm{d}\zeta + 2\gamma\nabla^2 Z + N, \tag{2.27}$$

where we have split the sum of the net normal surface forces and gravity into a surface tension term (with dimensionless parameter γ) and a net load N. However:

$$\int_{-(1/2)}^{1/2}\begin{pmatrix}\sigma_{xz} \\ \sigma_{yz}\end{pmatrix}\mathrm{d}\zeta = \frac{\partial}{\partial x}\begin{pmatrix}M_{xx} \\ M_{xy}\end{pmatrix} + \frac{\partial}{\partial y}\begin{pmatrix}M_{xy} \\ M_{yy}\end{pmatrix} + \begin{pmatrix}\Sigma_{xx} \\ \Sigma_{xy}\end{pmatrix}\frac{\partial Z}{\partial x} + \begin{pmatrix}\Sigma_{xy} \\ \Sigma_{yy}\end{pmatrix}\frac{\partial Z}{\partial y}, \tag{2.28}$$

where the moments are

$$\mathbf{M} = \begin{pmatrix}M_{xx} & M_{xy} \\ M_{xy} & M_{yy}\end{pmatrix} = \int_{-(1/2)}^{1/2}\zeta\begin{pmatrix}\sigma_{xx} & \sigma_{xy} \\ \sigma_{xy} & \sigma_{yy}\end{pmatrix}\mathrm{d}\zeta. \tag{2.29}$$

Hence the net normal force balance becomes

$$\begin{aligned}Re\frac{\partial W}{\partial t} = {} & \frac{\partial^2 M_{xx}}{\partial x^2} + 2\frac{\partial^2 M_{xy}}{\partial x \partial y} + \frac{\partial^2 M_{yy}}{\partial y^2} \\ & + \Sigma_{xx}\frac{\partial^2 Z}{\partial x^2} + 2\Sigma_{xy}\frac{\partial^2 Z}{\partial x \partial y} + \Sigma_{yy}\frac{\partial^2 Z}{\partial y^2} + 2\gamma\nabla^2 Z + N,\end{aligned} \tag{2.30}$$

where the first three terms on the right-hand side describe the bending force and the second three terms are related to the stretching force on the sheet.

(d) Constitutive laws

To establish the constitutive laws satisfied by the stress resultants and moments, we first define

$$I_{j,n}(\alpha,\Upsilon)=\int_{-(1/2)}^{1/2}(\Upsilon-\zeta)^j\left(\frac{\dot\gamma}{\dot\Gamma}\right)^{n-1}\mathrm{d}\zeta=\int_{-(1/2)}^{1/2}(\Upsilon-\zeta)^j[(\zeta-\Upsilon)^2+\alpha^2]^{(n-1)/2}\,\mathrm{d}\zeta. \tag{2.31}$$

Notably:

$$I_{0,0}=\sinh^{-1}\left(\frac{1-2\Upsilon}{2\alpha}\right)+\sinh^{-1}\left(\frac{1+2\Upsilon}{2\alpha}\right),\quad I_{0,1}=1,\quad I_{0,3}=\frac{1}{12}+\alpha^2+\Upsilon^2, \tag{2.32}$$

$$I_{0,2}=\frac{1}{2}\alpha^2 I_{0,0}+\frac{1}{8}(1+2\Upsilon)\sqrt{(1+2\Upsilon)^2+4\alpha^2}+\frac{1}{8}(1-2\Upsilon)\sqrt{(1-2\Upsilon)^2+4\alpha^2} \tag{2.33}$$

and

$$I_{1,n}=\frac{[(1+2\Upsilon)^2+4\alpha^2]^{(n+1)/2}-[(1-2\Upsilon)^2+4\alpha^2]^{(n+1)/2}}{2^{n+1}(n+1)},\quad I_{1,1}=\Upsilon \tag{2.34}$$

and, for $\alpha\to 0$,

$$I_{0,n}\to\frac{|1+2\Upsilon|^{n-1}(1+2\Upsilon)+|1-2\Upsilon|^{n-1}(1-2\Upsilon)}{2^n n}\quad\text{and}$$
$$I_{1,n}\to\frac{|1+2\Upsilon|^{n+1}-|1-2\Upsilon|^{n+1}}{2^{n+1}(n+1)}. \tag{2.35}$$

With these integrals, we may substitute equations (2.17) and (2.21) into (2.25) and (2.29), to find

$$\boldsymbol{\Sigma}=\Gamma^{n-1}[I_{0,n}\boldsymbol{\Delta}+(I_{1,n}-\Upsilon I_{0,n}))\boldsymbol{\Gamma}]+\frac{\mathrm{Bi}}{\Gamma}[I_{0,0}\boldsymbol{\Delta}+(I_{1,0}-\Upsilon I_{0,0})\boldsymbol{\Gamma}] \tag{2.36}$$

and

$$\begin{aligned}\mathbf{M}=\Gamma^{n-1}&\{(\Upsilon I_{0,n}-I_{1,n})\boldsymbol{\Delta}+[2\Upsilon I_{1,n}-I_{0,n+2}+(\alpha^2-\Upsilon^2)I_{0,n}]\boldsymbol{\Gamma}\}\\&+\frac{\mathrm{Bi}}{\Gamma}\{(\Upsilon I_{0,0}-I_{1,0})\boldsymbol{\Delta}+[2\Upsilon I_{1,0}-I_{0,2}+(\alpha^2-\Upsilon^2)I_{0,0}]\boldsymbol{\Gamma}\}.\end{aligned} \tag{2.37}$$

Equations (2.36) and (2.37) in combination with the kinematic conditions (which reduce to $W=\partial Z/\partial t$), (2.26) and (2.30) constitute the model equations for our viscoplastic plate. Before we apply this model to some specific examples, we first examine the general yield criteria that it incorporates.

(e) Plastic limit and yield conditions

In the plastic limit when we ignore viscous contributions, equations (2.36) and (2.37) reduce to

$$\left.\begin{aligned}\boldsymbol{\Sigma}&\to\frac{\mathrm{Bi}}{\Gamma}[I_{0,0}\boldsymbol{\Delta}+(I_{1,0}-\Upsilon I_{0,0})\boldsymbol{\Gamma}],\\ \mathbf{M}&\to\frac{\mathrm{Bi}}{\Gamma}\{(\Upsilon I_{0,0}-I_{1,0})\boldsymbol{\Delta}+[2\Upsilon I_{1,0}-I_{0,2}+(\alpha^2-\Upsilon^2)I_{0,0}]\boldsymbol{\Gamma}\}.\end{aligned}\right\} \tag{2.38}$$

From these relations, we may calculate the invariants:

$$\Sigma^2=\frac{1}{2}\left[\mathrm{Tr}(\boldsymbol{\Sigma}^2)-\frac{1}{3}\mathrm{Tr}(\boldsymbol{\Sigma})^2\right]=\frac{1}{3}(\Sigma_{xx}^2+\Sigma_{yy}^2-\Sigma_{xx}\Sigma_{yy})+\Sigma_{xy}^2, \tag{2.39}$$

$$M^2=\frac{1}{2}\left[\mathrm{Tr}(\mathbf{M}^2)-\frac{1}{3}\mathrm{Tr}(\mathbf{M})^2\right]=\frac{1}{3}(M_{xx}^2+M_{yy}^2-M_{xx}M_{yy})+M_{xy}^2 \tag{2.40}$$

and

$$\begin{aligned}\mathcal{X}&=\frac{1}{2}\left[\mathrm{Tr}(\mathbf{M}\boldsymbol{\Sigma})-\frac{1}{3}\mathrm{Tr}(\mathbf{M})\mathrm{Tr}(\boldsymbol{\Sigma})\right]\\&=\frac{1}{3}(M_{xx}\Sigma_{xx}+M_{yy}\Sigma_{yy})-\frac{1}{6}(M_{xx}\Sigma_{yy}+M_{yy}\Sigma_{xx})+M_{xy}\Sigma_{xy},\end{aligned} \tag{2.41}$$

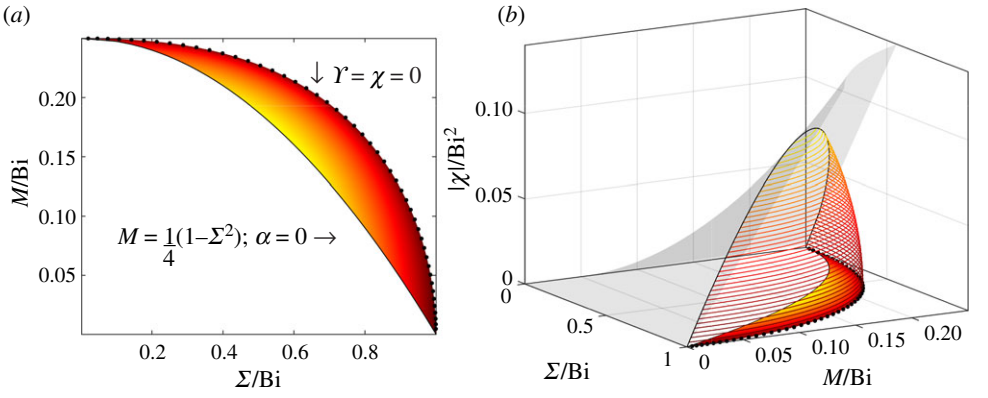

Figure 2. An illustration of the yield criteria in equation (2.42), showing $\mathcal{X}$ as (*a*) a density and (*b*) as a surface over the (Σ, M)-plane. The limits for $\alpha \to 0$ and $\Upsilon \to 0$ are highlighted, and the surface shaded grey shows $|\mathcal{X}| = M\Sigma$. (Online version in colour.)

to arrive at the conditions,

$$\left.\begin{aligned} \Sigma^2 &= \mathrm{Bi}^2(\alpha^2 I_{0,0}^2 + I_{1,0}^2), \quad \mathcal{X} = \mathrm{Bi}^2(\alpha^2 \Upsilon I_{0,0}^2 + \Upsilon I_{1,0}^2 - I_{1,0} I_{0,2}) \\ M^2 &= \mathrm{Bi}^2[\alpha^2(I_{1,0} - \Upsilon I_{0,0})^2 + (I_{0,2} - \Upsilon I_{1,0} - \alpha^2 I_{0,0})^2]. \end{aligned}\right\} \tag{2.42}$$

Together, these three relations dictate α, Υ and the yield condition under general combinations of bending moments and in-plane stresses, which feature through the invariants Σ, M and $\mathcal{X}$. Note that $\mathcal{X} \leq M\Sigma$, with the equality arriving when $\mathbf{M}$ and $\boldsymbol{\Sigma}$ are aligned.[1]

For $\alpha \to 0$, the bending moment and tension tensors become aligned ($\mathbf{M} \propto \boldsymbol{\Sigma}$), and the yield condition reduces to

$$M = \frac{1}{4}\mathrm{Bi}(1 - \Xi^2), \quad \Sigma = \mathrm{Bi}\Xi \quad \text{and} \quad \mathcal{X} = -M\Sigma, \tag{2.43}$$

where $\Xi = \min(1, 2|\Upsilon|)$. This condition coincides with the criterion derived in [18], given that $(V, \partial/\partial y, \alpha) \to 0$ for a beam, and $M = \frac{1}{2}|M_{xx}|$ and $\Sigma = \frac{1}{2}|\Sigma_{xx}|$. As pointed out above, this provides the largest value for $|\mathcal{X}|$ for a given moment M and tension Σ. The opposite limit, $\Upsilon \to 0$, or $\mathcal{X} \to 0$, corresponds to a curve on the (Σ, M)-plane given by the parametric form:

$$\Sigma = 2\alpha \mathrm{Bi} \sinh^{-1}\left(\frac{1}{2\alpha}\right) \quad \text{and} \quad M = \mathrm{Bi}\left[\frac{1}{4}\sqrt{1 + 4\alpha^2} - \alpha^2 \sinh^{-1}\left(\frac{1}{2\alpha}\right)\right]. \tag{2.44}$$

In pure bending $\mathbf{M} \to -\mathrm{Bi}\boldsymbol{\Gamma}/(4\Gamma)$, and the yield condition is simply

$$M^2 = \frac{1}{3}(M_{xx}^2 + M_{yy}^2 - M_{xx}M_{yy}) + M_{xy}^2 = \frac{\mathrm{Bi}^2}{16}. \tag{2.45}$$

This condition also follows immediately from the original, leading-order form of the Herschel–Bulkley model, given that $\sigma_{ij} \sim 4M_{ij}\,\mathrm{sgn}(\zeta)$ ($j = 1$ or 2), and corresponds to the von Mises criterion traditionally used for plates [3,7,22,40].

The general yield criterion in equation (2.42) is equivalent to that presented by Ilyushin [23,24], and corresponds to the parametrized form of a surface in $(\Sigma, M, \mathcal{X})$−space (the parameters being α and Υ). This surface is illustrated in figure 2, along with the limits $\alpha \to 0$ and $\Upsilon \to 0$ established above. Beyond this surface (to the right of the plot in figure 2*b*), the plate yields throughout its thickness (see §2c). Note that $|\mathcal{X}|$ is limited by the bound $M\Sigma$, restricting the accessible part of the $(\Sigma, M, \mathcal{X})$-space. Also, the plate yields for any moment when $\Sigma > \mathrm{Bi}$, or for any tension when $M > \frac{1}{4}\mathrm{Bi}$.

[1]For any symmetric matrix $\mathbf{A}$, the invariant $\frac{1}{2}[\mathrm{Tr}(\mathbf{A}^2) - \frac{1}{3}(\mathrm{Tr}\mathbf{A})^2] \geq 0$, and can only vanish if $\mathbf{A} = \mathbf{0}$. For $\mathbf{A} = \boldsymbol{\Sigma}\mathbf{M} - M\boldsymbol{\Sigma}\,\mathrm{sgn}(\mathcal{X})$, this implies that $2\Sigma M(\Sigma M - |\mathcal{X}|) \geq 0$, establishing the result.

3. Bending of rectangular plates without tension

If we discard the in-plane stress $\boldsymbol{\Sigma}$, strain rates $\mathbf{D}$ and force balance (2.26), the model reduces to

$$(\Upsilon,\alpha)\to 0,\quad \mathbf{M}\to -\left[\frac{\Gamma^{n-1}}{2^{n+1}(n+2)}+\frac{\mathrm{Bi}}{4\Gamma}\right]\boldsymbol{\Gamma}. \tag{3.1}$$

If we further omit surface tension $\gamma=0$ and adopt $n=1$, the viscous part of the bending force reduces to $-\frac{1}{12}\nabla^4 W$ (cf. [10,12]), and from equation (2.30) we arrive at the Bingham plate model:

$$Re\frac{\partial W}{\partial t}=-\frac{1}{3}\nabla^4 W-\frac{\partial^2}{\partial x^2}\left(\frac{\mathrm{Bi}\Gamma_{xx}}{4\Gamma}\right)-2\frac{\partial^2}{\partial x\partial y}\left(\frac{\mathrm{Bi}\Gamma_{xy}}{4\Gamma}\right)$$
$$-\frac{\partial^2}{\partial y^2}\left(\frac{\mathrm{Bi}\Gamma_{yy}}{4\Gamma}\right)+N,\quad \text{if } M>\frac{1}{4}\mathrm{Bi}, \tag{3.2}$$

the purely plastic version of which is the same as that used in the plasticity literature (e.g. [22]).

The failure of a flat, perfectly rigid-plastic rectangular plate satisfying the von Mises yield criterion has been attacked using limit analysis by [7,36–38] and references therein. This analysis places bounds on the critical value of the yield stress for which the plate fails. For a spatially uniform load (i.e. $N=1$) the sharpest existing computations indicate that (in our notation) $0.2086\lesssim \mathrm{Bi}_{\mathrm{crit}}\lesssim 0.2107$. For $\mathrm{Bi}<\mathrm{Bi}_{\mathrm{crit}}$, plastic failure occurs; for the viscoplastic fluid plates considered here, a finite plate velocity then arises that we may calculate using the augmented Lagrangian scheme outlined in appendix Aa.

A sample solution for a square plate with a uniform load ($N=1$) and $\mathrm{Bi}=\frac{1}{8}<\mathrm{Bi}_{\mathrm{crit}}$ is displayed in figure 3. The pattern of viscoplastic deformation is not very different from that of either a viscous or perfectly plastic plate (see panel (*b*), which shows two other solutions close to the Newtonian and plastic limits). A small plug appears in the corners of the plate if $\mathrm{Bi}>0$. A suite of computations with varying yield stress demonstrate that $W_{\max}$ converges (quadratically) to zero as Bi approaches a critical value around 0.21 (a more accurate estimate of $\mathrm{Bi}_{\mathrm{crit}}$ demands a higher spatial resolution than we use).

Results for rectangular plates are shown in figure 4. In these cases, the plate occupies $-1<x<1$ and $-L_y<y<L_y$, and is subjected to a spatially localized load with $N=(64/\pi)\,\mathrm{e}^{-16r^2}$, so that the forcing has a characteristic radius of $\frac{1}{4}$ and the net load is unity. For a square plate ($L_y=1$), this forcing generates a velocity W somewhat like that for the uniform load. However, the plate eventually plugs up further from the localized load for longer plates ($L_y>2.25$), with the solution becoming independent of L_y once the yielded region disconnects from the top and bottom edges (as illustrated by the midsection profiles of w in (*c*) and the speed and plug data plotted in (*d*) and (*e*)). The yielded region also detaches from the side edges ($x=\pm1$) for narrower plates ($L_y<0.5$), owing to the containment effect of the top and bottom clamping. For fixed yield stress Bi, this containment effect eventually triggers a passage to the plastic limit $\mathrm{Bi}\to\mathrm{Bi}_{\mathrm{crit}}(L_y)$, which occurs just below $\mathrm{Bi}=0.25$ for the examples shown in figure 4.

4. Bending of circular plates

For the bending of an axisymmetrical plate without tension, we first record the model equations written in polar coordinates (r,θ). These equations can be arrived at by following the reduction in §2c for the governing equations (2.8)–(2.15) expressed in cylindrical polars, or by using the transformation rules for tensors with the Cartesian model above:

$$Re\frac{\partial W}{\partial t}=\frac{\partial^2 M_{rr}}{\partial r^2}+\frac{2}{r}\frac{\partial M_{rr}}{\partial r}-\frac{1}{r}\frac{\partial M_{\theta\theta}}{\partial r}+N \tag{4.1}$$

and

$$\begin{pmatrix}M_{rr}\\M_{\theta\theta}\end{pmatrix}=-\left(\frac{\Gamma^{n-1}}{2^{n+1}(n+2)}+\frac{\mathrm{Bi}}{4\Gamma}\right)\begin{pmatrix}\Gamma_{rr}\\\Gamma_{\theta\theta}\end{pmatrix}\quad \text{for } M\equiv\sqrt{\frac{1}{3}(M_{rr}^2+M_{\theta\theta}^2-M_{rr}M_{\theta\theta})}>\frac{1}{4}\mathrm{Bi} \tag{4.2}$$

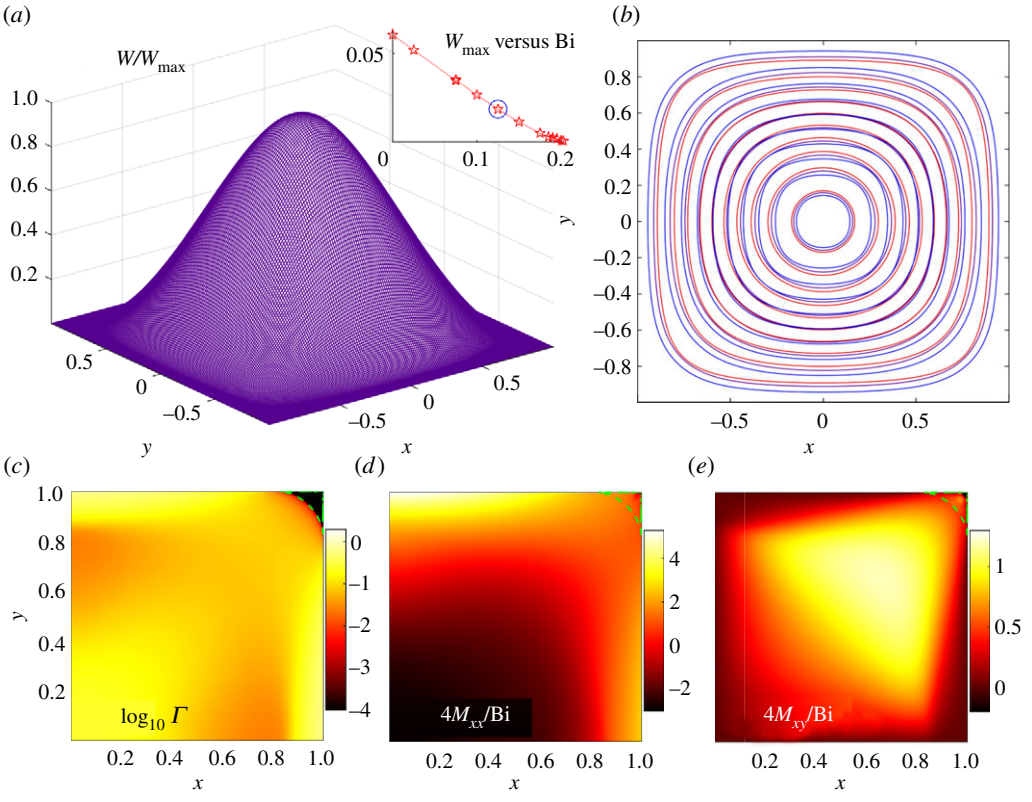

Figure 3. Pure bending solution for a (clamped) square plate subject to a uniform load with $\mathrm{Bi} = \frac{1}{8}$, showing (*a*) surface and (*b*) contour plots of $W/W_{\max}$, then density plots over the (x, y)-plane of (*c*) $\log_{10} \Gamma$, (*d*) $4M_{xx}/\mathrm{Bi}$ and (*e*) $4M_{xy}/\mathrm{Bi}$. In (*b*), we also show the contours for solutions with $\mathrm{Bi} = 10^{-4}$ (red) and $\mathrm{Bi} = 0.2$ (blue), and the sections through the midline $y = 0$ (original solution for $\mathrm{Bi} = \frac{1}{8}$ shown in purple). The inset in (*a*) displays $W_{\max}$ against Bi for a suite of computations. In (*c–e*), only the first quadrant is displayed and the dashed line indicates the yield surface that isolates the plugged corner. (Online version in colour.)

(and $\Gamma = 0$ otherwise), with

$$\Gamma_{rr} = 2\left(2\frac{\partial^2}{\partial r^2} + \frac{1}{r}\frac{\partial}{\partial r}\right)W, \quad \Gamma_{\theta\theta} = 2\left(\frac{\partial^2}{\partial r^2} + \frac{2}{r}\frac{\partial}{\partial r}\right)W, \quad \Gamma \equiv \sqrt{\frac{1}{3}(\Gamma_{rr}^2 + \Gamma_{\theta\theta}^2 - \Gamma_{rr}\Gamma_{\theta\theta})}. \tag{4.3}$$

The Bingham version of this model is equivalent to that proposed by Wierzbicki [25] (see his eqns (2.3)), although a linearization of the constitutive law is immediately adopted in that work for further analysis (which reduces the stress terms to a viscous-like biharmonic one; see also [26–28]). Although there are common points, the generalization of Wierzbicki's model stated in eqn (4.12) of [27] to a rate-dependent constitutive law is not the same as our Herschel–Bulkley model, which is more similar to plate models based on the Cowper–Symonds law used in structural mechanics [29]. In the plastic limit,

$$M_{rr}^2 + M_{\theta\theta}^2 - M_{rr}M_{\theta\theta} \to \frac{3}{16}\mathrm{Bi}^2, \tag{4.4}$$

and we recover the plastic plate model used by [3,40].

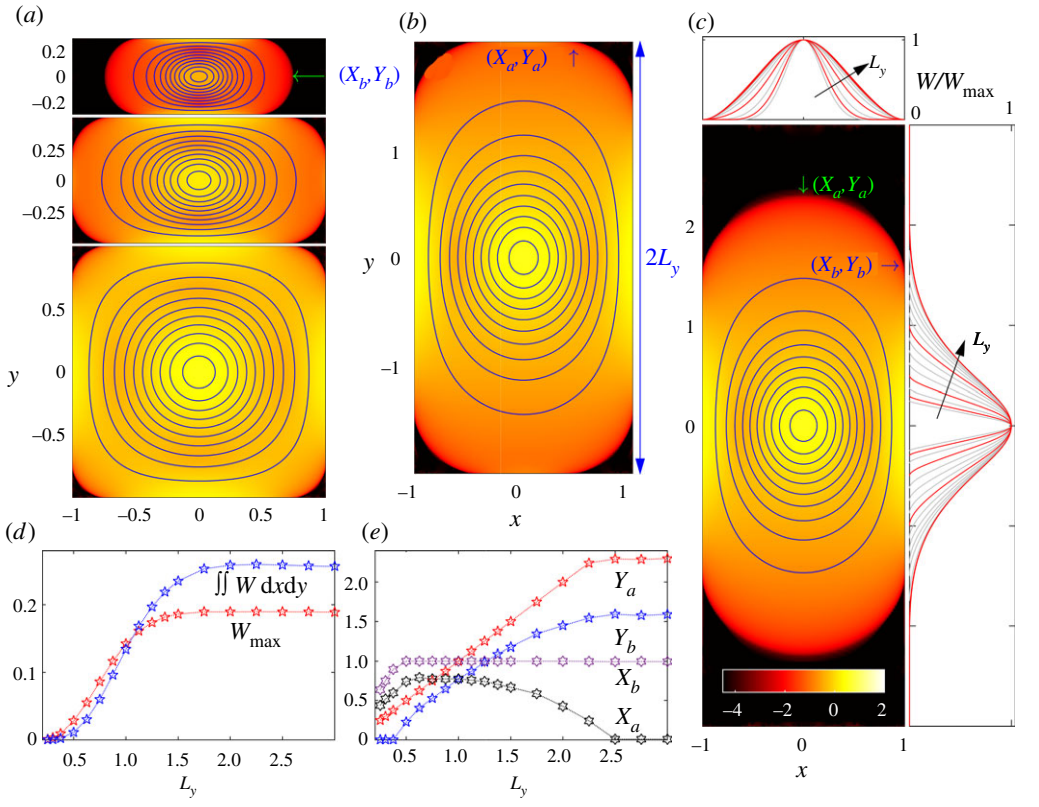

Figure 4. Pure bending solution for (clamped) rectangular plates subjected to a compact load with Bi $= \frac{1}{5}$. The plate occupies $-1 < x < 1$ and $-L_y < y < L_y$. In the upper panels we show density plots of $\log_{10} \Gamma$ over the (x, y)-plane, with superposed contours of constant $W/W_{\max}$, for (*a*) $L_y = 0.3$, $\frac{1}{2}$ and 1, (*b*) $L_y = 2$, and (*c*) $L_y = 3$. Midsections through the profiles along $y = 0$ (top) and $x = 0$ (right) are also plotted in (*c*); the darker (red) lines show the profiles for the solutions plotted as densities in (*a–c*), whereas profiles for all the other computed solutions are shown in lighter grey. The lower panels plot (*d*) $W_{\max}$ and $\iint W\,dx\,dy$, and (*e*) the uppermost and rightmost positions of the yielded region (X_a, Y_a) and (X_a, Y_a) (as indicated on the density plots), against L_y. (Online version in colour.)

(a) Failure states

For $Re \to 0$, we may compute the mode of failure of flat circular plates below the critical yield stress, $\mathrm{Bi} < \mathrm{Bi}_{\mathrm{crit}}$. Some results are shown in figures 5 and 6 for $N = 1$. The solutions are again computed using an augmented Lagrangian scheme (see appendix Ab). The first figure shows examples with $(M_{rr} - M_{\theta\theta}, W') \to 0$ for $r \to 0$ and $W(1) = W'(1) = 0$, corresponding to solutions for a circular plate that is clamped at its outer edge ($r = 1$); similar solutions for circular plates with simply supported edges ($M_{rr}(1) = 0$) have been reported in [27]. The second figure displays solutions for a clamped annulus ($W = W' = 0$ at both edges; inner radius at $r = \frac{1}{3}$).

The computations in figure 5 demonstrate the convergence to the purely plastic solution of the problem [3,40] which is encountered for $\mathrm{Bi} = \mathrm{Bi}_{\mathrm{crit}} \approx 0.184$. On approaching this limit,

$$W_{\max} \sim 6.37(\mathrm{Bi}_{\mathrm{crit}} - \mathrm{Bi})^2. \tag{4.5}$$

The origin of this scaling is rooted in the emergence of a viscoplastic boundary layer at the edge for $\mathrm{Bi} \to \mathrm{Bi}_{\mathrm{crit}}$, which is required because the solution in the plastic limit fails to satisfy the clamping condition $W'(1) = 0$. Over the viscoplastic boundary layer, or 'hinge', W_r varies sharply, adjusting the solution to meet the boundary condition and enforcing the limit $(M_{rr}, 2M_{\theta\theta}) \to -\frac{1}{2}\mathrm{Bi}_{\mathrm{crit}}$, which aligns with the boundary conditions adopted for the perfectly plastic solution [3,40]. We provide

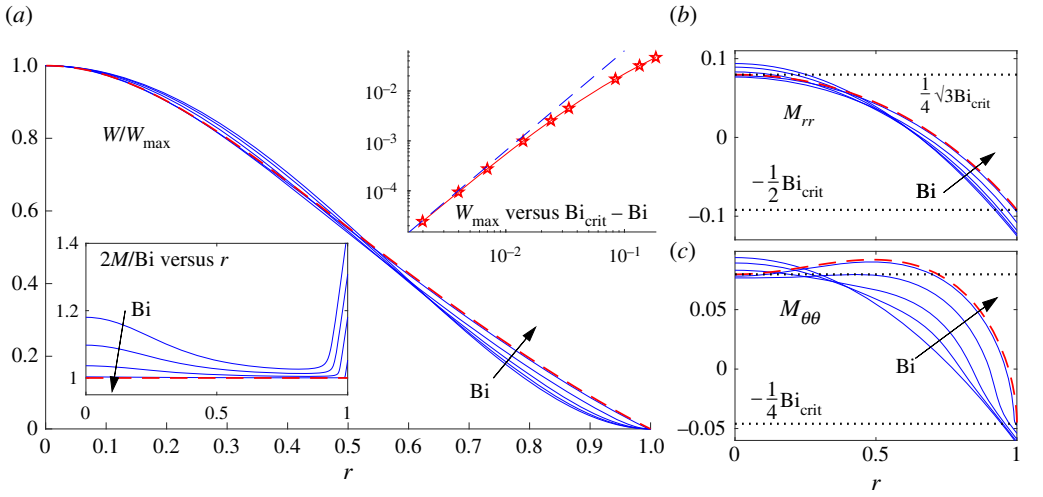

Figure 5. Pure bending solution for a circular plate clamped at its edge. (*a*) W/W_{max}, (*b*) M_{rr} and (*c*) $M_{\theta\theta}$ against r for $Bi = 10^{-4}$, 0.05, 0.10 0.15 and 0.18. The purely plastic solution at $Bi = Bi_{crit} \approx 0.184$ is shown by the dashed lines. The insets in (*a*) show W_{max} against $Bi_{crit} - Bi$, along with $6.37(Bi_{crit} - Bi)^2$, and $2M/Bi$ against r for $Bi = 0.15$, 0.16, 0.17 and 0.18. (Online version in colour.)

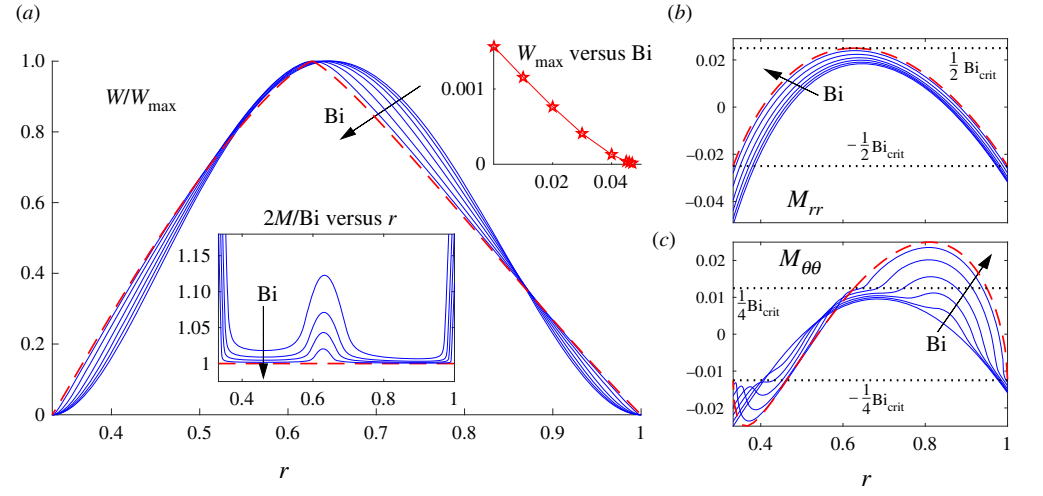

Figure 6. Pure bending solution for an annulus clamped at both edges with inner radius at $r = \frac{1}{3}$. (*a*) W/W_{max}, (*b*) M_{rr} and (*c*) $M_{\theta\theta}$ against r for $Bi = 10^{-4}$, 0.01, 0.02, 0.03, 0.04 and 0.047. The purely plastic solution at $Bi = Bi_{crit} \approx 0.050$ is shown by the dashed lines. The insets in (*a*) show W_{max} against Bi, and $2M/Bi$ against r for $Bi = 0.04$, 0.043, 0.45 and 0.47. (Online version in colour.)

a more detailed analysis of the hinge region in appendix B, establishing both the power and prefactor in equation (4.5).

The annulus solutions in figure 6 display convergence to another plastic limit, this time for $Bi = Bi_{crit} \approx 0.05$. Viscoplastic boundary layers again develop against the clamped edges, but a further hinge also appears at a radius r_h midway across the annulus where the radial bending moment M_{rr} reaches a maximum and $(M_{rr}, 2M_{\theta\theta}) \to \frac{1}{2}Bi_{crit}$. To compute the corresponding plastic limit, one must piece together two solutions, one for $[\frac{1}{3}, r_h]$ and the other for $[r_h, 1]$. At the clamped

edges, $(M_{rr}, 2M_{\theta\theta}) \to -\frac{1}{2}\mathrm{Bi}_{\mathrm{crit}}$, whereas $(M_{rr}, 2M_{\theta\theta}) \to \frac{1}{2}\mathrm{Bi}_{\mathrm{crit}}$, and $M'_{rr} = 0$ at the internal hinge, $r = r_h$. As detailed in appendix B, the viscoplastic boundary layers that arise at the clamped edges are thinner than the internal hinge and control the failure for $\mathrm{Bi} < \mathrm{Bi}_{\mathrm{crit}}$.

The failure states of the annulus are also interesting to compare against the corresponding states for a loaded flat beam (i.e. the initial fall of the viscoplastic catenary of [18]). For a beam, rigid plugs intervene between yielded sections at the centre and clamped edges (cf. figure 10 of appendix Aa). Over these plugs, the yield condition demands only that $\partial^2 W/\partial x^2 = 0$, allowing for the appearance of tilting sections with linear slopes for $W(x,t)$ and therefore $Z(x,t)$. For the curvilinear geometry of the circular plate, however, the yield condition $\Gamma = 2\sqrt{\frac{1}{2}(W'')^2 + \frac{1}{2}r^{-2}(W')^2 + \frac{1}{2}(W'' + r^{-1}W')^2} = 0$ demands that $W' = W'' = 0$ over the plugged regions. The tilting plugs of the beam are therefore ruled out for the radial problem and instead develop into regions of nearly perfectly plastic deformation for the circular plate (where $M \approx \frac{1}{2}\mathrm{Bi}$; see the inset of figure 6*a*).

(b) Impulsively driven inertial plates

Wang & Hopkins [39] considered the inertial deflection of a circular plate set impulsively into motion for a perfectly plastic material satisfying the Tresca yield condition. The viscoplastic version of the problem with the von Mises condition, corresponding to the current plate model for a Bingham fluid, was solved approximately by Wierzbicki [25] and Wierzbicki & Florence [26].

Numerical solutions for an impulsively and uniformly driven Bingham plate are shown in figures 7 and 8. In this problem, with no enduring load ($N = 0$), a convenient choice for the velocity scale $\mathcal{V}$ is the initial velocity, so that $W(r,0) = 1$ for $r < 1$. Equation (2.13*a*) then sets the stress scale $\mathcal{P}$. Moreover, in the absence of tension, we may avoid an explicit consideration of the Reynolds number on the dynamics by redefining t: the only time derivatives to appear are in the inertial term and the kinematic relation $W = \partial Z/\partial t$. Hence, if we switch to the time variable tRe^{-1}, the Reynolds number is only needed to reconstruct the deflection $Z(r,t)$ from the velocity $W(r,t)$. If we focus on $n = 1$, the Bingham number Bi becomes the only remaining parameter. Figure 7 shows the details of a solution with $\mathrm{Bi} = 1$, and a summary of results from a suite of computations with varying Bi; an example with higher yield stress, $\mathrm{Bi} = 100$, is displayed in figure 8.

As illustrated by the snapshots of W in figure 7*d*, the plate behaves viscously near the clamped edge at early times owing to the relatively large strain rates that arise there. Indeed, for $t \ll 1$, one expects the viscous arrest of the motion owing to clamping to take the form of a signal propagating into the plate with the self-similar form, $W = F(\eta)$ with $\eta = (1-r)(Re/t)^{1/4}$. This feature of the velocity deficit at the edge is well illustrated by the snapshots in figure 7*d* which are equally spaced in $t^{1/4}$. Despite this, the strain rates decline quickly into the bulk of the plate, and the associated bending moment M does not remain above the yield value $\frac{1}{2}\mathrm{Bi}$ much beyond the edge. The fluid then stays plugged up over a rapidly shrinking central area (see figure 7*a*, which shows the plug for an early time snapshot). At later times, the plug disappears, but re-emerges briefly whenever the radial gradients of W become small at the centre of the plate, which happens repeatedly owing to the spatially oscillating structure of the velocity deficit and whenever the profile at $r = 0$ passes through an inflexion. Finally, the plate deflection brakes to rest under the yield stress, with motion stopping in finite time (unlike for the viscous problem, where motion decays exponentially). A number of the finer details of the dynamics are not captured by the approximations employed in [25,26,28].

When $\mathrm{Bi} \gg 1$, the yield stress has more impact, as seen in the solution in figure 8. In this case, the velocity profile remains flat-topped over much of the evolution, bordered by a weaker internal viscoplastic hinge, with a sharper hinge appearing at the outer edge. The plot of the strain rate Γ on the space-time diagram in figure 8*b* illustrates the recurring plugs (which appear over the regions where the colour shading saturates at its lowest value). For $(t/Re)^{1/4} \gtrsim 0.14$, the flat top and its weak hinge disappears, leaving a rounded decaying profile. The two phases of evolution are evidently the analogue of those constructed in [39] for a perfectly plastic Tresca material.

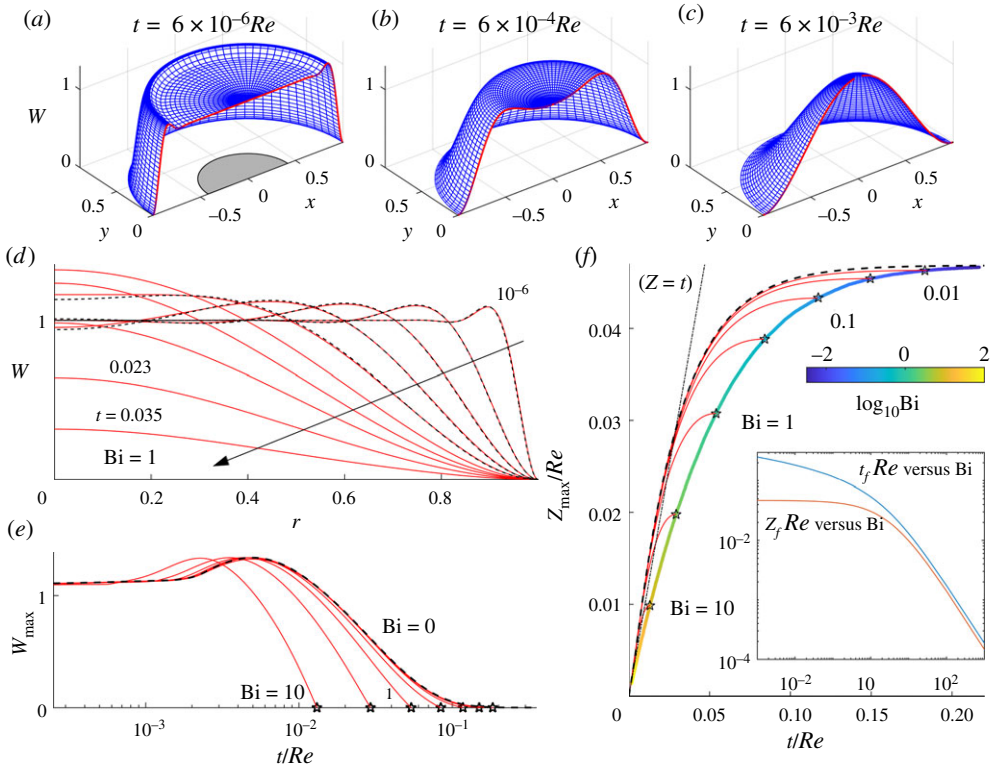

Figure 7. An impulsively driven clamped plate. (*a–c*) show snapshots of $W(r, t)$ at the times indicated for Bi = 1. In (*a*), the shaded region indicates the central plug. Further snapshots are plotted in (*d*), equally spaced in $t^{1/4}$; the black dashed lines show the corresponding viscous (Bi = 0) solution for the first five. Panels (*e*) and (*f*) show time series of maximum velocity W_{max} and scaled maximum displacement Z_{max}/Re (respectively) for solutions with $\mathrm{Bi} = 10^{(1/2)j-1}$ and $j = 0, 1, \ldots, 6$. The stars indicate the end points of the computations, and the dashed lines again show the viscous solution. In (*f*), the thicker line shows the end points of computations for more values of Bi, coloured according to the key indicated; the corresponding stopping times $t_f Re$ and maximum deflections $Z_f Re$ are plotted against Bi in the inset. (Online version in colour.)

Although the dynamics depend on Bi in this way, the profile of the final displacement is similar for all yield stresses, with Z/Z_{max} merely becoming steeper near the outer hinge for larger Bi (figure 8*d*). Note that the approximation for the scaled final profile provided in [26] is independent of Bi and corresponds to the viscous solution (for which $Z \to \frac{3}{64}(1-r^2)^2 Re$). The stopping times t_f and final deflections Z_f are plotted against Bi in the inset of figure 7*f* . In the plastic limit ($\mathrm{Bi} \gg 1$), we record the results

$$(t_f, Z_f) \sim (0.19, 0.15)\frac{Re}{\mathrm{Bi}}, \quad \text{or} \quad t_f \sim 0.19\frac{\rho \mathcal{V}^2 \mathcal{R}^2}{\mathcal{H}\tau_Y} \text{ and } Z_f \sim 0.15\frac{\rho \mathcal{V}^2 \mathcal{R}^2}{\mathcal{H}\tau_Y} \tag{4.6}$$

in dimensional units, where $\mathcal{R} \equiv \mathcal{L}$ is the plate radius and $\mathcal{V}$ the initial velocity (cf. [26,29,39], who quote similar formulae, but with pre-factors of 0.4 and 0.3, respectively).

5. Bending beams with tension

In our last example, we include in-plane stresses and strain rates for a (one-dimensional) beam without inertia and surface tension ($Re = \gamma = 0$). With $\partial/\partial y \to 0$ and $V \to 0$, we find $\alpha \to 0$ and the

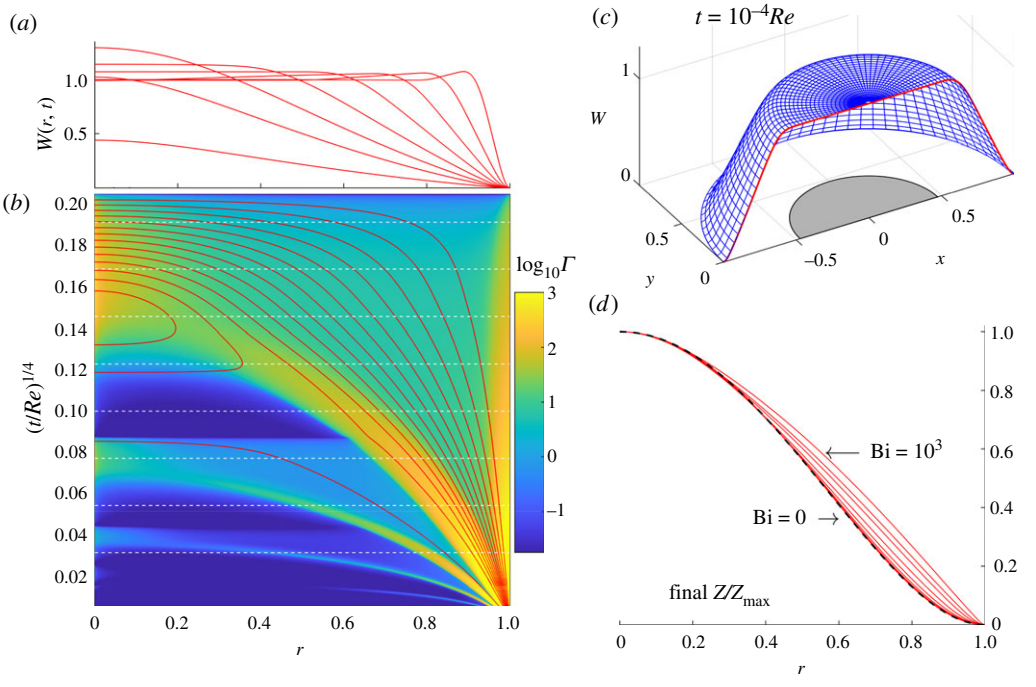

Figure 8. An impulsively driven clamped plate with Bi = 100, showing (*a*) snapshots of $W(r, t)$ equally spaced in $t^{1/4}$, (*b*) the strain rate $\log_{10}\Gamma$ plotted as a density on the $(r, t^{1/4})$-plane with superposed contours of constant W, and (*c*) a surface plot of $W(r, t)$ at $t = 10^{-4}Re$ with the plug shaded grey. The dashed lines in (*b*) indicate the times of the snapshots in (*a*). In (*d*), we compile the final profiles of $Z/Z_{\max}$ for the current solution, all the computations in figure 7, and two more solutions with $\mathrm{Bi} = 10^{1.5}$ and 10^3. The dashed line again shows the viscous solution. (Online version in colour.)

plate model becomes, where the plate is yielded and $\Sigma_{xx}^2 + 8\mathrm{Bi}|M_{xx}| > 4\mathrm{Bi}^2$,

$$\left.\begin{aligned}
&\Sigma_{xx} = \frac{|1+2\Upsilon|^{n+1} - |1-2\Upsilon|^{n+1}}{(n+1)\Upsilon}\left|\frac{\partial^2 W}{\partial x^2}\right|^{n-1} D_{xx} \\
&\quad + 2\mathrm{Bi}\,\Xi\ \mathrm{sgn}(D_{xx}), \quad \Xi = \min(1, 2|\Upsilon|), \\
&M_{xx} = -\left[\Lambda\left|\frac{\partial^2 W}{\partial x^2}\right|^n + \frac{1}{2}\mathrm{Bi}(1-\Xi^2)\right]\mathrm{sgn}\left(\frac{\partial^2 W}{\partial x^2}\right), \quad D_{xx} = \frac{\partial U}{\partial x} + \frac{\partial Z}{\partial x}\frac{\partial W}{\partial x}, \\
&\Lambda = \frac{(1+n-2\Upsilon)|1+2\Upsilon|^{n+1} + (1+n+2\Upsilon)|1-2\Upsilon|^{n+1}}{2(n+1)(n+2)}, \quad \Upsilon = D_{xx}\left(\frac{\partial^2 W}{\partial x^2}\right)^{-1}, \\
&\text{and} \quad \frac{\partial \Sigma_{xx}}{\partial x} = 0, \quad \frac{\partial^2 M_{xx}}{\partial x^2} + \Sigma_{xx}\frac{\partial^2 Z}{\partial x^2} + N = 0,
\end{aligned}\right\} \tag{5.1}$$

as in [18] (if $\Sigma_{xx}^2 + 8\mathrm{Bi}|M_{xx}| < 4\mathrm{Bi}^2$, $D_{xx} = \partial^2 W/\partial x^2 = 0$). We use this model to explore the deflection of an initially flat beam (i.e. $W(x, 0) = Z(x, 0) = 0$) under a localized load with

$$N(x) = \frac{1}{x_c} \times \begin{cases} 1, & |x| < x_c \\ 0, & |x| > x_c \end{cases}. \tag{5.2}$$

Provided $\mathrm{Bi} < \mathrm{Bi}_{\mathrm{crit}} \equiv 1 - \frac{1}{2}x_c$, the beam fails, but then comes to rest once the deflection builds up the in-plane tension. The dynamics are illustrated by the sample numerical solutions of equations (5.1) displayed in figure 9 for the case of a compactly loaded Bingham plate ($x_c \to 0$ and $n = 1$).

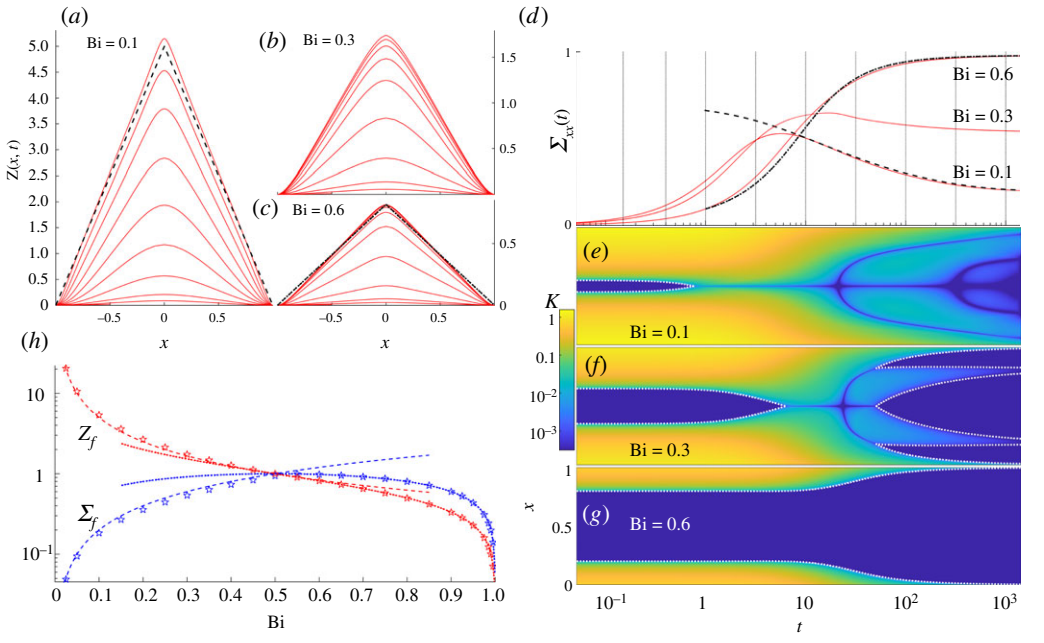

Figure 9. Deflections of a beam under a localized load ($x_c = 0$). Snapshots of $Z(x, t)$ are shown for (*a*) Bi = 0.1, (*b*) Bi = 0.3 and (*c*) Bi = 0.6. In (*d*), we show the corresponding time series of the tensions $\Sigma(t)$, and in (*e–g*) the distributions of the bending rate $K = |\partial^2 W/\partial x^2|$ as densities over the (x, t)-plane for the right half of the beam. The dotted lines in (*d*) indicate the times of the snapshots in (*a–c*), and the light dotted lines in (*e–g*) locate the borders of the plugs. Results for a wider range of yield stress are shown in (*h*), which plots the final tension Σ_f and maximum deflection Z_f against Bi (stars). The dashed lines in (*a*,*d*) and (*h*) indicate the predictions of the analysis in §5a (equations (5.6) and (5.7), taking $\Sigma_{xx}(0) = 0.7$); the dot-dashed lines show the results from §5b (equations (5.19) and (5.20), taking $\Sigma_{xx}(1)$ from the numerical solution as initial condition). (Online version in colour.)

Initially the beam contains two plugs symmetrically placed about the centre, occupying $x_a < |x| < x_b$. For lower yield stresses, the plugs narrow and disappear, to leave a fully yielded beam. At higher yield stress, the plugs persist and widen, leaving narrow viscoplastic hinges against the clamped edges. For $x_c > 0$, the central yield region narrows with time, but remains wider than the hinges at the clamped ends (cf. [18]). However, for a compact load, and as seen in figure 9, the central region thins to another viscoplastic hinge at $x = 0$. With an intermediate yield stress, the evolution is more convoluted, with the plugs disappearing, then others appearing at different positions within the beam, see figure 9*f* . The limits of lower and larger yield stress can be understood analytically, as we map out below.

(a) Fully yielded beams

When $\mathrm{Bi} \ll 1$, the beam becomes fully yielded after an initial transient (figure 9*e*) and approaches its final state over a relatively long timescale. The final phase of evolution is characterized by the scalings

$$t = O(\mathrm{Bi}^{-2-(1/n)}), \quad (\Sigma, U, \Delta_{xx}) = O(\mathrm{Bi}), \quad (W, M) = O(\mathrm{Bi}^2), \quad (Z, \Upsilon) = O(\mathrm{Bi}^{-1}).$$

Under these scalings, the normal force balance implies

$$\Sigma_{xx}\frac{\partial^2 Z}{\partial x^2} \sim -N(x) \quad \text{and} \quad Z \sim \Sigma_{xx}^{-1} \times \begin{cases} 1 - \frac{1}{2}x_c - x^2/(2x_c), & 0 \le x \le x_c \\ 1 - x, & x_c \le x \le 1 \end{cases}. \tag{5.3}$$

Bearing in mind that $\Upsilon \gg 1$, we have $\Xi = 1$, and so the constitutive law implies that

$$\Sigma_{xx} \sim 2^{2n} |D_{xx}|^{n-1} D_{xx} + 2\mathrm{Bi}, \tag{5.4}$$

(given that $(D_{xx}, \Sigma_{xx}) > 0$). From equation (5.3) we may compute $W = \partial Z/\partial t$ and then

$$\Delta_{xx} \sim 4\frac{\partial U}{\partial x} - \frac{4\dot{\Sigma}_{xx}}{{x_c}^2 \Sigma_{xx}^3} \times \begin{cases} x^2 & 0 \le x \le x_c \\ {x_c}^2 & x_c \le x \le 1 \end{cases}. \tag{5.5}$$

Integrating over the beam and imposing $U \to 0$ at $x = 0$ and $x = 1$, we find

$$\dot{\Sigma}_{xx} \sim -\frac{3\Sigma_{xx}^3 (\Sigma_{xx} - 2\mathrm{Bi})^{1/n}}{4(3 - 2x_c)}, \tag{5.6}$$

which implies a final tension and maximum deflection of

$$\Sigma_f \sim 2\mathrm{Bi} \quad \text{and} \quad Z_f \sim (2\mathrm{Bi})^{-1}. \tag{5.7}$$

These predictions are compared with numerical results in figure 9.

(b) Bending near the plastic limit

Closer to the critical yield stress $\mathrm{Bi}_{\mathrm{crit}}$, the deflection of the beam is controlled by the viscoplastic hinges that develop against the clamped ends ($x = \pm 1$), with an internal hinge at the centrepoint ($x = 0$) permitting the bulk of the two sides of the beam to tilt rigidly (cf. figure 9*c*,*g*). Over the rigid sections, we have

$$Z \sim Z_{\max}(1 - |x|), \quad \frac{\partial Z}{\partial x} \sim -Z_{\max}, \quad \frac{\partial W}{\partial x} \sim -\dot{Z}_{\max}. \tag{5.8}$$

We also have $D_{xx} = 0$ over the plug, implying

$$\frac{\partial U}{\partial x} \sim -\frac{\partial Z}{\partial x}\frac{\partial W}{\partial x} \quad \text{and} \quad U|_{x\to 1} \sim U|_{x\to 0} - Z_{\max}\dot{Z}_{\max}, \tag{5.9}$$

where the limits refer to the approach of the plug solution to the hinges.

Within the hinges, the viscous bending term $\Lambda|\partial^2 W/\partial x^2|^n$ becomes important, but viscous stretching remains too small to matter (as it features one less spatial derivative). Thus, $\Sigma/(2\mathrm{Bi}) = \Xi$ is constant in x over both hinges, given that $\partial \Sigma_{xx}/\partial x = 0$. There can also be no plugs if $\Xi = 1$ (the beam yielding entirely under any moment), and so $\Xi = 2|\Upsilon|$. Over the internal hinge at the centre, $\Upsilon = D_{xx}(\partial^2 W/\partial x^2)^{-1} < 0$ (the rate of extension must be positive, but the curvature rate is negative). Moreover, since Z and W become small for $x \to 1$:

$$D_{xx} \sim \frac{\partial U}{\partial x} \sim \frac{\Sigma_{xx}}{4\mathrm{Bi}}\frac{\partial^2 W}{\partial x^2}. \tag{5.10}$$

Hence, an integral over the hinge provides

$$U|_{x\to 0} \sim \frac{\Sigma_{xx}\dot{Z}_{\max}}{4\mathrm{Bi}}, \tag{5.11}$$

given that $\partial W/\partial x$ must match with equation (5.8c) and $U = \partial W/\partial x = 0$ at $x = 0$. By contrast, $\Upsilon > 0$ over the hinge at the clamped end, the stretching and curvature rates both now being positive. Hence, a similar argument implies

$$U|_{x\to 1} \sim -\frac{\Sigma_{xx}\dot{Z}_{\max}}{4\mathrm{Bi}}. \tag{5.12}$$

It follows immediately from equations (5.9), (5.11) and (5.12) that $Z_{\max} \sim \Sigma_{xx}/(2\mathrm{Bi})$.

A finer analysis is needed to account for bending over the hinges at the clamped ends, requiring the matched asymptotic expansion of appendix B. We avoid the details here, however,

identifying only the salient points. First, the constitutive law for the hinge at $x = 1$ indicates that

$$M_{xx} + \frac{1}{2}\mathrm{Bi}(1 - \Xi^2) \sim -\Lambda \left(\frac{\partial^2 W}{\partial x^2}\right)^n, \tag{5.13}$$

where the factor Λ is constant in x since $\Upsilon \to \Sigma_{xx}/(4\mathrm{Bi})$ (N.B. in appendix B, $\Lambda \to (n+2)^{-1}$ and $\Xi \to 0$). Next, if bending over the internal hinge at $x = 0$ is not important (cf. appendix B), the normal-force balance implies that

$$M_{xx} \sim \frac{1}{2}\mathrm{Bi}(1 - \Xi^2) + \Sigma(Z_{\max} - Z) - \frac{1}{2} \times \begin{cases} x^2/x_c, & |x| < x_c \\ (2x - x_c), & x_c < |x| \end{cases} \tag{5.14}$$

$$\to -\frac{1}{2}\mathrm{Bi}(1 - \Xi^2) + \left(1 - \frac{\Sigma^2}{2\mathrm{Bi}}\right)(1 - x) - \tilde{M} \quad \text{for } x \to 1, \tag{5.15}$$

where

$$\tilde{M} = 1 - \mathrm{Bi} - \frac{\Sigma^2}{4\mathrm{Bi}} - \frac{1}{2}x_c \tag{5.16}$$

is a small residual moment that drives evolution and must be balanced by the viscous bending stress at the edge of the beam. Hence, the bending profile of the hinge is given by

$$\frac{\partial^2 W}{\partial x^2} \sim \left(\frac{2\mathrm{Bi} - \Sigma^2}{2\mathrm{Bi}\Lambda}\right)^{1/n} (x - x_p)^{1/n}, \quad x_p = 1 - \frac{2\mathrm{Bi}\tilde{M}}{2\mathrm{Bi} - \Sigma^2}, \tag{5.17}$$

(cf. appendix B). However, the only detail required to complete the solution outside the hinge is the bending rate, $\partial W/\partial x$, at the edge of the hinge ($x = x_p$), which follows immediately from integrating equation (5.17) and must match with $\partial W/\partial x$ from (5.8c).

Assembling the preceding results, we arrive at an evolution equation for the tension:

$$\dot{\Sigma}_{xx} \sim \frac{4n\mathrm{Bi}^2\Lambda^{-(1/n)}}{(n+1)(2\mathrm{Bi} - \Sigma_{xx}^2)}\left(\mathrm{Bi}_{\mathrm{crit}} - \mathrm{Bi} - \frac{\Sigma^2}{4\mathrm{Bi}}\right)^{1+(1/n)} \quad \left(\mathrm{Bi}_{\mathrm{crit}} \equiv 1 - \frac{1}{2}x_c\right). \tag{5.18}$$

This equation applies if $x_c > 0$, implying the central hinge is weaker than those at the ends (appendix B). If $x_a \to 0$, on the other hand, bending is also significant within the central hinge, driven by the sharpness of the load. In that circumstance, the contribution of the viscous stress for $x \ll 1$ must also be included in equation (5.14), but as the problem becomes symmetrical about $x = \frac{1}{2}$ in this limit (figure 9), this addition simply amounts to replacing the left-hand side of equation (5.16) by $2\tilde{M}$. Consequently, for $x_c \to 0$ and $n = 1$:

$$\dot{\Sigma}_{xx} \sim \frac{3[4\mathrm{Bi}(1 - \mathrm{Bi}) - \Sigma_{xx}^2]^2}{32(2\mathrm{Bi} - \Sigma_{xx}^2)}. \tag{5.19}$$

An approximation of this equation, that works slightly better for lower Bi and Σ_{xx}, is to neglect Σ_{xx}^2 in comparison to 2Bi in the denominator, as employed in figure 9 along with the predictions for the final tension and maximum deflection:

$$\Sigma_f \sim \sqrt{4\mathrm{Bi}(1 - \mathrm{Bi})} \quad \text{and} \quad Z_f \sim \sqrt{\mathrm{Bi}^{-1} - 1}. \tag{5.20}$$

6. Discussion

In this paper, we have developed a theory for the bending of thin plates of viscoplastic fluid described by the Herschel–Bulkley law. Our outlook is somewhat different from that in solid mechanics, where viscoplastic models have been used previously to describe metal plates (e.g. [25–27,29]), our main aim being to apply the theory to a number of geophysical problems. The construction follows on from developments in plasticity [2–4,22] and viscous fluid mechanics [9–12], and builds on earlier analyses of viscoplastic beams [17–20]. The Herschel–Bulkley law employs the von Mises yield criterion, which complicates the analysis of the dynamics of a thin

plate and previously prompted many in plasticity theory to opt for other yield criteria (e.g. [2–6,22,43]). However, armed with modern numerical and asymptotic methods, there is no need to avoid the von Mises condition in plate theory. Indeed, the plate model we have developed here conveniently poses the yield criterion in terms of three particular invariants of the bending moment and in-plane stress tensors. This yield criterion is equivalent to that presented by Ilyushin [23,24], and compactly organizes the interaction between the various stress components for the geometry of a thin plate. With the plate model in hand, we have reconsidered a number of classical problems concerning the failure of viscoplatic plates or their deflection under load. The formulation is well suited to numerical and further asymptotic analysis. To assist with the former, we have adapted an augmented Lagrangian algorithm that deals consistently with any unyielded regions and the singularity in the effective viscosity at yield [41,42].

Data accessibility. The MATLAB codes to generate the data shown in the figures are submitted as electronic supplementary material. The titles and captions for the files are also submitted as electronic supplementary material.

Authors' contributions. Both T.V.B. and N.J.B. contributed equally to the analysis, the numerical computations and preparing the manuscript.

Competing interests. We declare we have no competing interests.

Funding. No funding has been received for this article.

Acknowledgements. We thank Duncan Hewitt for helpful discussions on the numerical schemes used.

Appendix A. Augmented Lagrangian schemes ($n = 1$)

The augmented Lagrangian scheme is based on a variational formulation of the problem and avoids difficulties with the yield condition by introducing dummy variables and an iterative algorithm. A key feature is to reduce the original problem to a linear, inhomogeneous, biharmonic-type problem for W at each step of the iteration. Our viscoplastic plate model corresponds to the Euler–Lagrange equations associated with variations of the augmented functional:

$$\mathcal{F}_*[W,\boldsymbol{\lambda},\mathbf{k}] = \int\int \left(\frac{1}{24}\Gamma^2 + \frac{1}{4}\mathrm{Bi}\gamma - NW\right)\mathrm{d}x\mathrm{d}y + \int\int \sum_{i,j}\left[\lambda_{ij}(K_{ij}-k_{ij}) + \frac{1}{2}\varpi(K_{ij}-k_{ij})(\Gamma_{ij}-\gamma_{ij})\right]\mathrm{d}x\mathrm{d}y, \tag{A 1}$$

where ϖ is a relaxation parameter and $\boldsymbol{\gamma} = 2\mathbf{k} + 2\mathrm{Tr}(\mathbf{k})\mathbf{I}$, or $\mathbf{k} = \frac{1}{2}\boldsymbol{\gamma} - \frac{1}{6}\mathrm{Tr}(\boldsymbol{\gamma})\mathbf{I}$. The functional derivatives give

$$\left(\frac{1}{3} + 4\varpi\right)\nabla^4 W = N - \sum_{i,j}\frac{\partial^2}{\partial x_i \partial x_j}[\lambda_{ij} - \varpi\gamma_{ij}] \tag{A 2}$$

and

$$\boldsymbol{\gamma} = \begin{cases} \mathbf{0}, & T < \frac{1}{4}\mathrm{Bi} \\ \varpi^{-1}\left(1 - \frac{1}{4}T^{-1}\mathrm{Bi}\right)\mathbf{T}, & \text{otherwise} \end{cases}, \qquad \begin{aligned} &\mathbf{T} = \boldsymbol{\lambda} + \varpi\boldsymbol{\Gamma}, \\ &T = \tfrac{1}{2}\mathrm{Tr}(\mathbf{T}^2) - \tfrac{1}{6}\mathrm{Tr}(\mathbf{T})^2, \end{aligned} \tag{A 3}$$

and $K_{ij} = k_{ij}$, which are solved iteratively as outlined below.

(a) Rectangular plates in pure bending

Building on the preceding Euler–Lagrange equations, the iteration loop is

$$\left(\frac{1}{3}+4\varpi\right)\nabla^4 W^{(j+1)} = 1 - \frac{\partial^2}{\partial x^2}(\lambda_{xx}^{(j)} - \varpi\gamma_{xx}^{(j)}) - \frac{\partial^2}{\partial x\partial y}(\lambda_{xy}^{(j)} - \varpi\gamma_{xy}^{(j)}) - \frac{\partial^2}{\partial y^2}(\lambda_{yy}^{(j)} - \varpi\gamma_{yy}^{(j)}), \tag{A 4}$$

$$\boldsymbol{\Gamma}^{(j+1)} = 2\mathbf{K}^{(j+1)} + 2\mathrm{Tr}(\mathbf{K}^{(j+1)})\mathbf{I}, \quad K_{ij}^{(j+1)} = \frac{\partial^2 W^{(j+1)}}{\partial x_i \partial x_j}, \tag{A 5}$$

$$\boldsymbol{\gamma}^{(j+1)} = \begin{cases} \mathbf{0}, & T < \frac{1}{4}\mathrm{Bi} \\ \varpi^{-1}\left(1 - \frac{1}{4}T^{-1}\mathrm{Bi}\right)\mathbf{T}, & \text{otherwise} \end{cases}, \quad \begin{array}{c} \mathbf{T} = \boldsymbol{\lambda}^{(j)} + \varpi\boldsymbol{\Gamma}^{(j+1)}, \\ T = \frac{1}{2}\mathrm{Tr}(\mathbf{T}^2) - \frac{1}{6}\mathrm{Tr}(\mathbf{T})^2, \end{array} \tag{A 6}$$

and

$$\boldsymbol{\lambda}^{(j+1)} = \boldsymbol{\lambda}^{(j)} + \varpi(\boldsymbol{\Gamma}^{(j+1)} - \boldsymbol{\gamma}^{(j+1)}). \tag{A 7}$$

where the superscript refers to iterate. To solve equation (A 4) at each step, we use Chebyshev differentiation matrices that directly incorporate the boundary conditions on W [44]. We choose $\varpi = \frac{1}{2}\mathrm{Bi}$ for one-dimensional beams $\varpi = 8\mathrm{Bi}$ for square plates (the scheme ought to converge for any value of this parameter, but empirical tests indicate these choices to be expedient). The iteration loop is continued until the root mean square differences in $W^{(j+1)} - W^{(j)}$ and $\boldsymbol{\Gamma}^{(j)} - \boldsymbol{\gamma}^{(j)}$ decline below 10^{-8} (for beams) or 10^{-4} (for plates) relative to the root-mean-square averages of $W^{(j)}$ and $\Gamma^{(j+1)}$, respectively.

Figure 10 compares a sample numerical solution for a clamped flat beam with the exact solution [18]. The overall rate of convergence is relatively fast except close to the plastic limit (which is $\mathrm{Bi} = \mathrm{Bi}_{\mathrm{crit}} = 0.5$ for this problem). The solution contains two plugs spaced symmetrically about the centre (spanning $x < |x_a|$ and $x_b < |x| < 1$) over which the stress state is formally indeterminate for the full plate problem. The augmented Lagrangian algorithm nevertheless converges to an admissible solution within any plugs. For the square plate solutions shown in figure 3, we employ 120×120 collocation points distributed over $0 \leq (x, y) \leq 1$, exploiting the symmetry about $x = y = 0$ to restrict the computational grid to the first quadrant. We employ a similar reduction for the rectangular plates in figure 4 and use the same number of collocation points.

The numerical scheme used in §5 does not employ an augmented Lagrangian scheme. Instead, the model in equation (5.1) with $n = 1$ is sufficiently simple to solve directly: at each time step, we invert the constitutive law to write D_{xx} and $\partial^2 W/\partial x^2$ in terms of Σ_{xx} and M_{xx}, thereby incorporating the yield condition. We may then integrate equation (5.1) in space, given the current deflection $Z(x, t)$; we use MATLAB's bvp4c for this task. The predicted velocity $W(x, t)$ can then be used to evolve the defection to the next time step using forward Euler.

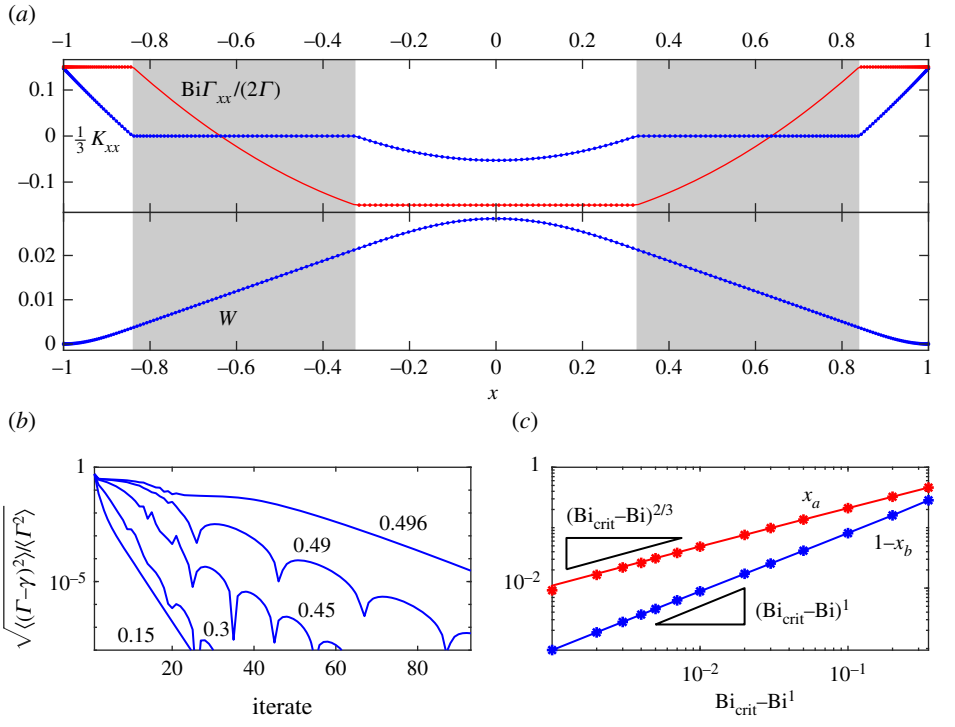

Figure 10. Pure bending solution for a clamped flat beam with Bi = 0.3, showing (*a*) $W, K_{xx}/3$ and $\mathrm{Bi}\,\Gamma_{xx}/4\Gamma$. The lines show the computed solution with 120 Chebyshev points distributed over [0, 1], the symmetry about $x = 0$ having been exploited to halve the computational domain; the dots indicate the exact solution (evaluated at the collocation points). The shaded regions indicate the plugs, $|x| < x_a$ and $x_b < |x| < 1$. Panel (*b*) shows the convergence of $\langle \Gamma^{(j+1)} - \gamma^{(j+1)} \rangle / \langle \Gamma^{(j+1)} \rangle$ against j for the values of Bi indicated ($\langle \cdots \rangle$ denoting root-mean-square average). In (*c*), we plot $1 - x_b$ and x_a against $\mathrm{Bi}_{\mathrm{crit}} - \mathrm{Bi}$ for the numerical solutions (stars) and analytical solution (lines). (Online version in colour.)

(b) Circular plates

The augmented Lagrangian scheme for the axisymmetrical problem is:

$$\frac{1}{r}\frac{\partial^2}{\partial r^2}[rM_{rr}^{(j+1)}] - \frac{1}{r}\frac{\partial M_{\theta\theta}^{(j+1)}}{\partial r} + N = \frac{Re}{\Delta t}(W^{j+1} - W_p), \tag{A 8}$$

$$\begin{pmatrix} M_{rr}^{(j+1)} \\ M_{\theta\theta}^{(j+1)} \end{pmatrix} = -\left(\frac{1}{12} + \varpi\right)\boldsymbol{\Gamma}^{(j+1)} - \boldsymbol{\lambda}^{(j)} + \varpi\boldsymbol{\gamma}^{(j)},$$

$$\boldsymbol{\gamma}^{(j)} = \begin{pmatrix} \gamma_{rr}^{(j)} \\ \gamma_{\theta\theta}^{(j)} \end{pmatrix}, \quad \boldsymbol{\lambda}^{(j+1)} = \begin{pmatrix} \lambda_{rr}^{(j+1)} \\ \lambda_{\theta\theta}^{(j+1)} \end{pmatrix}, \tag{A 9}$$

$$\boldsymbol{\Gamma}^{(j+1)} = \begin{pmatrix} \Gamma_{rr}^{(j+1)} \\ \Gamma_{\theta\theta}^{(j+1)} \end{pmatrix}, \quad \Gamma_{rr}^{(j+1)} = 2\left(2\frac{\partial}{\partial r} + \frac{1}{r}\right)\frac{\partial W^{(j+1)}}{\partial r}, \quad \Gamma_{\theta\theta}^{(j+1)} = 2\left(\frac{\partial}{\partial r} + \frac{2}{r}\right)\frac{\partial W^{(j+1)}}{\partial r},$$

along with equations (A 6) and (A 7). When the inertial term is included ($Re \neq 0$), the backward Euler differencing of the time derivative in equation (A 8) introduces the solution from the previous time step, denoted W_p, leading to a fully implicit marching scheme; Δt is the duration of the time step.

We solve this problem using MATLAB's bvp4c to integrate equations (A 8) and (A 9) at each step of the iteration; the inhomogeneous terms stemming from $\boldsymbol{\gamma}^{(j)}$ and $\boldsymbol{\lambda}^{(j)}$ are known during this integration and need only to be tabulated and then interpolated over a suitably fine reference

grid. The method has the advantage of exploiting an adaptive grid to place gridpoints wherever the solution for $W^{(j+1)}$ changes sharply. We make the convenient choice $\varpi = 2\mathrm{Bi}$.

Note that the sample solutions in figures 5 and 6 yield either everywhere (for $\mathrm{Bi} < \mathrm{Bi}_{\mathrm{crit}}$) or nowhere (for $\mathrm{Bi} > \mathrm{Bi}_{\mathrm{crit}}$). In such cases, we may use a simple integrator without any yield condition to provide a useful check on the fidelity of the numerical solutions or to accelerate their computation. Alternatively, we may also 'regularize' the constitutive law [21] by including a small parameter ε in $\Gamma^2 = \frac{1}{3}(\Gamma_{rr}^2 + \Gamma_{\theta\theta}^2 - \Gamma_{rr}\Gamma_{\theta\theta} + \varepsilon^2)$. This latter algorithm proves convenient when plugs appear as in the inertial plate problem of figure 7, and furnishes solutions (for $\varepsilon = 0.005$ or less) in agreement with those from the augmented Lagrangian algorithm, except for the stress over the plugs (where the regularized solutions are not completely rigid).

Appendix B. Viscoplastic boundary layers (hinges)

For $\mathrm{Bi} \to \mathrm{Bi}_{\mathrm{crit}}$, the bulk of the plate deforms like a perfectly plastic solid, with viscous stresses becoming restricted to narrow viscoplastic boundary layers, or 'hinges'. These layers arise against the clamped edges of the plate and around the loci of maximum deformation, and are the viscoplastic analogue of the hinges lines and circles that have received special attention in plasticity theory (e.g. [2,4–6,22,43,45]). The boundary layers may border rigid plugs or regions of nearly perfectly plastic deformation, and correspond to the fine structures found in other viscoplastic flow problems [46].

In the view of the shortened lengthscale around the hinge, the local bending rates are dominated by the component $\partial^2 W/\partial\eta^2$, where η denotes the normal coordinate to the hinge (i.e. either $\eta = r$ for the circular plate, or the Cartesian coordinate perpendicular to the edge of a rectangular plate). Thus, $\Gamma_{\eta\eta} = 2\Gamma_{\varsigma\varsigma}$ and $M_{\eta\eta} = 2M_{\varsigma\varsigma}$, if ς denotes the coordinate along the hinge. The solution for the bulk of the plate must therefore satisfy the leading-order boundary conditions $(M_{\eta\eta}, M_{\varsigma\varsigma}, M_{\varsigma\eta}) \to \pm\mathrm{Bi}(\frac{1}{2}, \frac{1}{4}, 0)$ at the hinge, selecting the plus sign for a velocity maximum, and the minus sign at a clamped edge.

(a) Clamped edges

Let $\delta \ll 1$ denote the reduced lengthscale of a hinge against a clamped edge. The deformation outside the hinge region is characterized by a solution $W = W_{\max} w_p$ of the purely plastic equations, where the shape function, $w_p(x, y)$ or $w_p(r)$, is prescribed but the amplitude $W_{\max} \ll 1$ is not. Instead, $W_{\max}$ is dictated by the viscous dissipation over the hinge region, leading to a limiting form $W_* \sim O(\mathrm{Bi}_{\mathrm{crit}} - \mathrm{Bi})^a$, where a can be determined from scaling theory. In particular, the contribution of the viscous stress to the bending moment is $O(\delta^{-2n}\Delta^n)$ if Δ denotes the variation in W across the hinge. This contribution must match the adjustment to the moment owing to the finite scale of the hinge region (i.e. $O(\delta)$), and the correction to the plastic bending moment stemming from the discrepancy between the yield stress and its critical value (i.e. $\mathrm{Bi}_{\mathrm{crit}} - \mathrm{Bi}$). That is, $\Delta^n/\delta^{2n} \sim \delta \sim O(\mathrm{Bi}_{\mathrm{crit}} - \mathrm{Bi})$, or $\delta \equiv \mathrm{Bi}_{\mathrm{crit}} - \mathrm{Bi}$ and $\Delta \sim O(\delta^{2+(1/n)})$. The amplitude $W_{\max}$ now follows from demanding that the bending rate in the bulk of the plate, $W_{\max}\partial w_p/\partial n = O(W_{\max})$, match with that in from hinge, which is $O(\delta^{-1}\Delta)$. Hence, $W_{\max} = O(\mathrm{Bi}_{\mathrm{crit}} - \mathrm{Bi})^{1+(1/n)}$. For $n = 1$, we arrive at $W_{\max} = O(\mathrm{Bi}_{\mathrm{crit}} - \mathrm{Bi})^2$, as observed in numerical computations (figures 3, 5 and 6).

Armed with these scalings, we now pursue a more detailed solution: we first note that over the bulk of the plate, the viscous bending stresses are $O(\delta^{1+n})$ or smaller given that $W \sim O(W_{\max})$ and length scales are $O(1)$. To $O(\delta)$, we may therefore assume that the solution is simply the perfectly rigid-plastic one, but with a yield stress $\mathrm{Bi} = \mathrm{Bi}_{\mathrm{cit}} - \delta$.

We next resolve the hinge region by rescaling the normal coordinate η and plate speed: $\eta = \delta\xi$ and $W = \delta^{2+(1/n)}\mathcal{W}(\xi)$ (taking the clamped edge to lie along $\eta = 0$). From the constitutive law:

$$M_{\eta\eta} \sim -\frac{1}{2}\mathrm{Bi} - \frac{(\partial^2\mathcal{W}/\partial\xi^2)^n}{(n+2)}\delta. \tag{B 1}$$

Once expressed in the local coordinates (ς, η), the force balance equation demands that

$$\delta^{-2}\frac{\partial^2 M_{\eta\eta}}{\partial \xi^2} + 2\delta^{-1}\frac{\partial^2 M_{\varsigma\eta}}{\partial \xi \partial \varsigma} + \delta^{-1}\kappa\frac{\partial}{\partial \xi}(2M_{\eta\eta} - M_{\varsigma\varsigma}) \sim O(1), \tag{B 2}$$

where κ is the curvature of the hinge. The local moment $M_{\eta\eta}$ must therefore be a linear function of ξ to $O(\delta^2)$ with the form

$$M_{\eta\eta} = -\frac{1}{2}\mathrm{Bi} - \delta C(\xi_* + \xi), \tag{B 3}$$

for some constants C and ξ_* which must be fixed by matching the hinge solution to the perfectly rigid-plastic one beyond. We now find the velocity profile:

$$\mathcal{W} = \frac{n}{n+1}[(n+2)C]^{1/n}\left[\frac{n(\xi_* + \xi)^{2+(1/n)}}{1+2n} - \frac{n\xi_*^{2+(1/n)}}{1+2n} - \xi\xi_*^{1+(1/n)}\right], \tag{B 4}$$

in view of the clamping conditions $\mathcal{W}(0) = \mathcal{W}'(0) = 0$. Finally, we note that the boundary layer ends for $\xi \to -\xi_*$ (where $\mathcal{W}'' \to 0$), where we may conveniently enforce a match. In particular, it follows that

$$W_{\max} = -\frac{n\xi_*^{1+(1/n)}[(n+2)C]^{1/n}}{(1+n)[\partial w_p/\partial n]_{n=0}}\delta^{1+(1/n)}. \tag{B 5}$$

For a circular plate, the structure of the perfectly plastic solution within the bulk of the plate permits further progress: this solution can be expressed in the form,

$$M_{\eta\eta} \equiv M_{rr} = \mathrm{Bi}F\left(\frac{r}{\sqrt{\mathrm{Bi}}}\right), \tag{B 6}$$

where the function $F(\zeta)$ satisfies $F \to -\frac{1}{2}$ and $F' \to -\frac{1}{4}(2 - \mathrm{Bi})\sqrt{\mathrm{Bi}}$ for $\zeta = \mathrm{Bi}_{\mathrm{crit}}^{-(1/2)}$. Thus, if $\mathrm{Bi} = \mathrm{Bi}_{\mathrm{crit}} - \delta$ and $r = 1 + \delta\xi$, it follows that

$$M_{rr} \sim -\frac{1}{2}\mathrm{Bi} - \frac{1}{4}\delta(2 - \mathrm{Bi}_{\mathrm{crit}})\left(\xi + \frac{1}{2\mathrm{Bi}_{\mathrm{crit}}}\right). \tag{B 7}$$

In other words, $\xi_* \equiv (2\mathrm{Bi}_{\mathrm{crit}})^{-1}$ and $C \equiv \frac{1}{4}(2 - \mathrm{Bi}_{\mathrm{crit}})$. The numerical plastic solution also indicates that $\mathrm{Bi}_{\mathrm{crit}} \approx 0.184$ and $\partial w_p/\partial r \approx -0.790$, leading to the prediction in equation (4.5) for $n = 1$.

(b) Internal hinges

For an internal hinge, the normal bending moment $M_{\eta\eta}$ also reaches a maximum at $\frac{1}{2}\mathrm{Bi}$, and its local form must therefore be quadratic: $M_{\eta\eta} \sim \frac{1}{2}\mathrm{Bi} + O(\eta^2)$. In the scaling analysis, we must then demand the balance $\Delta^n/\delta^{2n} \sim \delta^2$, or $\Delta \sim \delta^{2+(2/n)}$. The match of the bending rates at the edge of the hinge layer now implies that $W_{\max} \sim \delta^{-1}\Delta \sim \delta^{1+(2/n)}$. However, we always apply clamped conditions around the edges, so that $W_{\max} = O(\mathrm{Bi}_{\mathrm{crit}} - \mathrm{Bi})^{1+(1/n)}$. Thus, the internal hinge has a scale $\delta = O(\mathrm{Bi}_{\mathrm{crit}} - \mathrm{Bi})^{(1+n)/(2+n)}$, which is wider than the boundary layer at the clamped edge. A direct consequence of this feature is that the speed $W_{\max}$ beyond failure is dictated by the latter rather than the former. For $n = 1$, the internal hinge has thickness $\delta = O(\mathrm{Bi}_{\mathrm{crit}} - \mathrm{Bi})^{\frac{2}{3}}$, in comparison to the $O(\mathrm{Bi}_{\mathrm{crit}} - \mathrm{Bi})$ scale at the clamped edge. This disparity is evident in the inset of figure 6*a*, where the bending moment M over the boundary layers at the edge of a clamped annulus is both stronger and sharper than over the central hinge, and in the scalings for a loaded clamped beam shown in figure 10*c*.

References

1. Timoshenko SP, Woinowsky-Krieger S. 1959 *Theory of plates and shells*. New York, NY: McGraw-Hill.
2. Prager W, Hodge PG. 1951 *Theory of perfectly plastic solids*. New York, NY: Wiley.

3. Hopkins HG, Wang AJ. 1955 Load-carrying capacities for circular plates of perfectly-plastic material with arbitrary yield condition. *J. Mech. Phys. Solids* **3**, 117–129. (doi:10.1016/0022-5096(55)90055-7)
4. Hopkins HG, Prager W. 1954 On the dynamics of plastic circular plates. *Z. Angew. Math. Phys. ZAMP* **5**, 317–330. (doi:10.1007/BF01587827)
5. Mansfield EH. 1957 Studies in collapse analysis of rigid-plastic plates with a square yield diagram. *Proc. R. Soc. Lond. A* **241**, 311–338. (doi:10.1098/rspa.1957.0130)
6. Sawczuk A, Hodge P. 1968 Limit analysis and yield-line theory. *J. Appl. Mech.* **35**, 357. (doi:10.1115/1.3601203)
7. Hodge P, Belytschko T. 1968 Numerical methods for the limit analysis of plates. *J. Appl. Mech.* **35**, 796. (doi:10.1115/1.3601308)
8. Taylor G. 1969 Instability of jets, threads, and sheets of viscous fluid. In *Applied Mechanics: Proc. of the Twelfth Int. Congr. of Applied Mechanics, Stanford University* (eds M Hetenyi, WG Vincenti), pp. 382–388. Berlin, Germany: Springer.
9. Buckmaster J, Nachman A, Ting L. 1975 The buckling and stretching of a viscida. *J. Fluid Mech.* **69**, 1–20. (doi:10.1017/S0022112075001279)
10. Howell P. 1996 Models for thin viscous sheets. *Eur. J. Appl. Math.* **7**, 321–343. (doi:10.1017/S0956792500002400)
11. Ribe N. 2001 Bending and stretching of thin viscous sheets. *J. Fluid Mech.* **433**, 135–160. (doi:10.1017/S0022112000003360)
12. Ribe N. 2002 A general theory for the dynamics of thin viscous sheets. *J. Fluid Mech.* **457**, 255–283. (doi:10.1017/S0022112001007649)
13. Ribe N, Habibi M, Bonn D. 2012 Liquid rope coiling. *Annu. Rev. Fluid Mech.* **44**, 249–266. (doi:10.1146/annurev-fluid-120710-101244)
14. Mahadevan L, Keller JB. 1999 Periodic folding of thin sheets. *SIAM Rev.* **41**, 115–131. (doi:10.1137/S0036144598339166)
15. Teichman J, Mahadevan L. 2003 The viscous catenary. *J. Fluid Mech.* **478**, 71–80. (doi:10.1017/S0022112002003038)
16. Slim A, Balmforth N, Craster R, Miller J. 2008 Surface wrinkling of a channelized flow. *Proc. R. Soc. A* **465**, 123–142. (doi:10.1098/rspa.2008.0142)
17. Kamrin K, Mahadevan L. 2012 Soft catenaries. *J. Fluid Mech.* **691**, 165–177. (doi:10.1017/jfm.2011.466)
18. Balmforth N, Hewitt I. 2013 Viscoplastic sheets and threads. *J. Non-Newt. Fluid Mech.* **193**, 28–42. (doi:10.1016/j.jnnfm.2012.05.007)
19. Prior C, Moussou J, Chakrabarti B, Jensen OE, Juel A. 2016 Ribbon curling via stress relaxation in thin polymer films. *Proc. Natl Acad. Sci. USA* **113**, 1719–1724. (doi:10.1073/pnas.1514626113)
20. Hewitt I, Balmforth N. 2021 Viscoelastic ribbons. *J. Fluid Mech* **908**, A5. (doi:10.1017/jfm.2020.870)
21. Balmforth NJ, Frigaard I, Ovarlez G. 2014 Yielding to stress: recent developments in viscoplastic fluid mechanics. *Annu. Rev. Fluid Mech.* **46**, 121–146. (doi:10.1146/annurev-fluid-010313-141424)
22. Lubliner J. 2008 *Plasticity theory*. Mineola, NY: Dover Publications.
23. Robinson M. 1971 A comparison of yield surfaces for thin shells. *Int. J. Mech. Sci.* **13**, 345–354. (doi:10.1016/0020-7403(71)90059-2)
24. Robinson M. 1973 The effect of transverse shear stresses on the yield surface for thin shells. *Int. J. Solids Struct.* **9**, 819–828. (doi:10.1016/0020-7683(73)90005-X)
25. Wierzbicki T. 1967 Impulsive loading of rigid viscoplastic plates. *Int. J. Solids Struct.* **3**, 635–647. (doi:10.1016/0020-7683(67)90013-3)
26. Wierzbicki T, Florence A. 1970 A theoretical and experimental investigation of impulsively loaded clamped circular viscoplastic plates. *Int. J. Solids Struct.* **6**, 553–568. (doi:10.1016/0020-7683(70)90030-2)
27. Perzyna P. 1966 Fundamental problems in viscoplasticity. *Adv. Appl. Mech.* **9**, 243–377. (doi:10.1016/S0065-2156(08)70009-7)
28. Kelly JM, Wilshaw T. 1968 A theoretical and experimental study of projectile impact on clamped circular plates. *Proc. R. Soc. Lond. A* **306**, 435–447. (doi:10.1098/rspa.1968.0160)
29. Jones N. 2011 *Structural impact*. Cambridge, UK: Cambridge University Press.
30. Griffiths RW, Fink JH. 1993 Effects of surface cooling on the spreading of lava flows and domes. *J. Fluid Mech.* **252**, 667–702. (doi:10.1017/S0022112093003933)

31. Castruccio A, Rust A, Sparks R. 2013 Evolution of crust-and core-dominated lava flows using scaling analysis. *Bull. Volcanol.* **75**, 1–15. (doi:10.1007/s00445-012-0681-2)
32. Brož P *et al.* 2020 Experimental evidence for lava-like mud flows under Martian surface conditions. *Nat. Geosci.* **13**, 403–407. (doi:10.1038/s41561-020-0577-2)
33. Feltham DL. 2008 Sea ice rheology. *Annu. Rev. Fluid Mech.* **40**, 91–112. (doi:10.1146/annurev.fluid.40.111406.102151)
34. Sutherland BR, Balmforth NJ. 2019 Damping of surface waves by floating particles. *Phys. Rev. Fluids* **4**, 014804. (doi:10.1103/PhysRevFluids.4.014804)
35. Sauret A, Boulogne F, Cappello J, Dressaire E, Stone HA. 2015 Damping of liquid sloshing by foams. *Phys. Fluids* **27**, 022103. (doi:10.1063/1.4907048)
36. Le CV, Gilbert M, Askes H. 2009 Limit analysis of plates using the EFG method and second-order cone programming. *Int. J. Numer. Methods Eng.* **78**, 1532–1552. (doi:10.1002/nme.2535)
37. Le CV, Askes H, Gilbert M. 2010 Adaptive element-free Galerkin method applied to the limit analysis of plates. *Comput. Methods Appl. Mech. Eng.* **199**, 2487–2496. (doi:10.1016/j.cma.2010.04.004)
38. Bleyer J, De Buhan P. 2013 On the performance of non-conforming finite elements for the upper bound limit analysis of plates. *Int. J. Numer. Methods Eng.* **94**, 308–330. (doi:10.1002/nme.4460)
39. Wang AJ, Hopkins HG. 1954 On the plastic deformation of built-in circular plates under impulsive load. *J. Mech. Phys. Solids* **3**, 22–37. (doi:10.1016/0022-5096(54)90036-8)
40. Eason G. 1958 Velocity fields for circular plates with the von Mises yield condition. *J. Mech. Phys. Solids* **6**, 231–235. (doi:10.1016/0022-5096(58)90028-0)
41. Wachs A. 2007 Numerical simulation of steady Bingham flow through an eccentric annular cross-section by distributed Lagrange multiplier/fictitious domain and augmented Lagrangian methods. *J. Non-Newt. Fluid Mech.* **142**, 183–198. (doi:10.1016/j.jnnfm.2006.08.009)
42. Wachs A. 2019 Computational methods for viscoplastic fluid flows. In *Lectures on visco-plastic fluid mechanics* (eds G Ovarlez, S Hormozi), pp. 83–125. Berlin, Germany: Springer.
43. Collins I. 1971 On an analogy between plane strain and plate bending solutions in rigid/perfect plasticity theory. *Int. J. Solids Struct.* **7**, 1057–1073. (doi:10.1016/0020-7683(71)90080-1)
44. Trefethen LN. 2000 *Spectral methods in MATLAB*. Philadelphia, PA: SIAM.
45. Hopkins H. 1957 On the plastic theory of plates. *Proc. R. Soc. Lond. A* **241**, 153–179. (doi:10.1098/rspa.1957.0120)
46. Balmforth N, Craster R, Hewitt D, Hormozi S, Maleki A. 2017 Viscoplastic boundary layers. *J. Fluid Mech.* **813**, 929. (doi:10.1017/jfm.2016.878)